U.PORTO
FACULDADE DE CIÊNCIAS
UNIVERSIDADE DO PORTO

MSc

2nd
CYCLE

FCUP
2015

U.PORTO

Nanofriction Triboelectric Energy Harvesting

Carla Alexandra da Silva Alves

FC

U.PORTO
FACULDADE DE CIÊNCIAS
UNIVERSIDADE DO PORTO

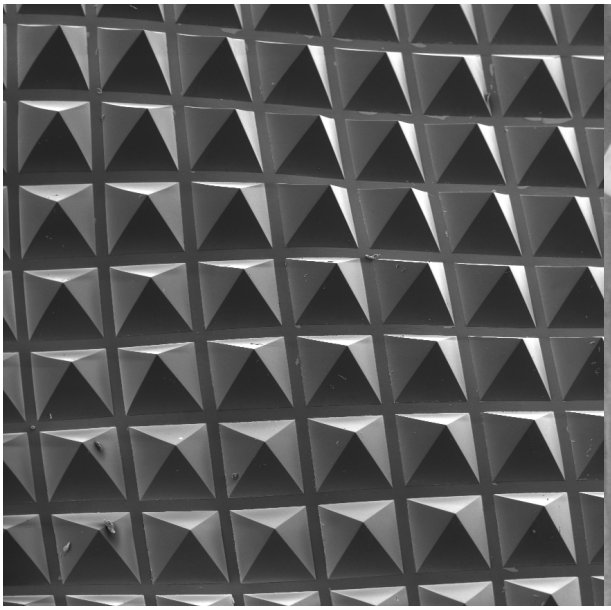
Nanofriction Triboelectric Energy Harvesting

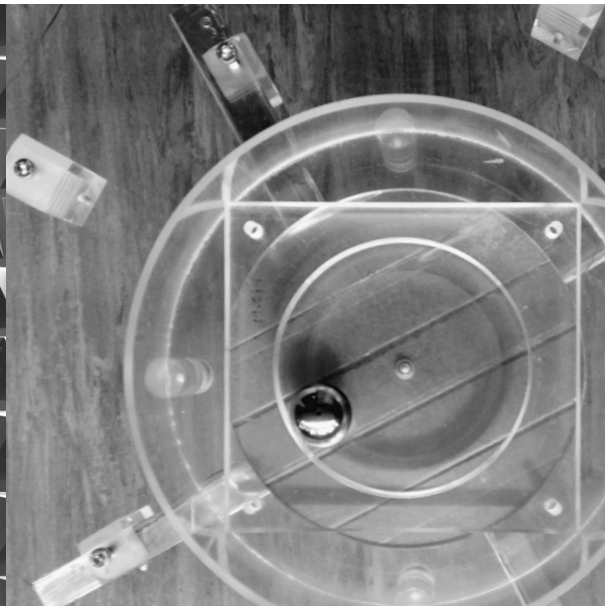
Carla Alexandra da Silva Alves

Master's Dissertation submitted to the
Faculty of Sciences of the University of Porto in
Engineering Physics

2015

MSc





Nanofriction Triboelectric Energy Harvesting

Carla Alexandra da Silva Alves
Integrated Master's in Engineering Physics
Physics and Astronomy Department
2015

Supervisor
João Oliveira Ventura, Auxiliar Researcher, Faculty of Sciences of the University of Porto

Co-Supervisor
André Miguel Trindade Pereira, Auxiliar Professor and Researcher, Faculty of Sciences of the University of Porto



All modifications determined by the Jury, and only those, were made.

The president of the Jury,

Porto, _____/_____/_____

“It is the mark of an educated mind to be able to entertain a thought without accepting it.”

Aristotle

Acknowledgements

First and foremost I would like to thank my supervisors Dr. João Ventura and Dr. André Pereira for all the help, support and mostly for all the motivation, that made me believe in myself and my abilities, and, of course, for the ever present optimism, even in the most dire situations. It was an excellent opportunity, as well as an enriching experience, which I will never forget. I want to let out that this was all really meaningful to me, so my deepest and most sincere thank you!

I want to mention Eng. Francisco Carpinteiro and Technician Fernando, for helping me carry on with my project and for all the availability and patience during its development. For all the help with all the electronic and computer issues, Eng. Pedro, and specially for the vast knowledge passed on to me, which was a large portion of everything I have learnt during this whole project. An enormous thank you for both Eng. Francisco Carpinteiro and Eng. Pedro, for the motivation and friendship.

For all the friendship, companionship and counsel, I want to leave a special thanks to my colleages and, above all, friends, Cátia Rodrigues, José Cardoso, Luís Costa, Pedro Resende, Bernardo Bordalo and Filipe Falcão.

Unquestionably, I owe my deepest gratitude to Diogo Costa and Mariana Lemos, for the massive help, patience and dedication.

Lastly, but certainly not least, to my family, whose limitless support and trust made all this come true, and without them none of this would be possible.

Resumo

O meio ambiente está repleto de fontes de energia que pode ser recolhida e convertida em eletricidade, como por exemplo, calor dissipado, deformações mecânicas, cargas estáticas, entre outras. Atendendo a este facto, surgiram dispositivos auto-alimentados, os chamados nanogeradores. São dispositivos promissores, uma vez que possibilitam a substituição, por exemplo, das baterias tradicionais. Em particular, os nanogeradores triboelétricos são dispositivos de grande interesse pois a sua produção é simples, de baixo custo e proporciona elevadas densidades de potência. O seu princípio de funcionamento é baseado nos efeitos de eletrificação e indução eletrostática, ou seja, o efeito triboelétrico, que é um fenómeno mundialmente conhecido. No entanto, a explicação do efeito ainda não está bem definida, tornado-se assim num tema de bastante interesse.

Existe uma enorme variedade de materiais que têm um comportamento triboeletrico inerente. Estes materiais têm a propriedade de ficarem eletricamente carregados através da fricção com outros materiais triboelétricos, criando uma carga positiva ou negativa à sua superfície, dependendo da tendência que possuem para perder ou ganhar eletrões. Um nanogerador triboelétrico, basicamente, é composto por dois materiais triboelétricos com diferentes polaridades, um "spacer" entre eles e dois elétrodos metálicos. Quando as superfícies dos materiais entram em contacto, é criada uma diferença de potencial entre os materiais, e por sua vez entre os elétrodos, originando o fluxo de eletrões entre estes, o que se traduz na produção de energia. De forma a melhorar os materiais triboelétricos, aumentando por sua vez o desempenho dos nanogeradores, é possível alterar a morfologia das suas superfícies.

Sendo o objetivo deste projecto a construção de um protótipo de um dispositivo triboelétrico, em primeiro lugar foi desenvolvido um sistema de testes para estudar as caraterísticas dos materiais triboelétricos disponíveis de forma a implementar no dispositivo o melhor par triboelétrico. Com este sistema de testes foi também possível verificar que, com os materiais micro- e nano- texturizados, são obtidos melhores resultados verificando-se um evidente aumento dos picos de tensão para o dobro. Desta forma, depois de escolhido o melhor par triboelétrico, foi possível proceder ao desenvolvimento de um dispositivo que usufrui da força magnética de uma bola ferromagnética e um íman para produzir energia. A média obtida para este dispositivo dos picos de tensão em circuito aberto foi de 4.2 V, a corrente de curto-circuito de ~ 6.3 μA e a densidade máxima de potência de 0.04 W/m^2. Todo este projeto contribui para o desenvolvimento e otimização de geradores triboelétricos num futuro próximo.

Abstract

There is a large amount of energy sources in our living environment, such as dissipated heat, mechanical deformation and static charges, which can be harvested and converted into electricity. With this in mind, self-powered nanosystems, the so-called nanogenerators (NGs), have been developed with the possibility of substituting the traditional power supplies, such as batteries. Particularly, the triboelectric nanogenerators (TENGs) are based on the contact electrification effect and on electrostatic induction, i.e. the triboelectric effect, which is an universally known phenomena.

There are plenty of choices of materials since almost of them have an inherent triboelectric behaviour. A triboelectric nanogenerator is composed basically by two triboelectric materials with different polarities, a spacer between them and two metal electrodes. The contact between two materials with different triboelectric polarities result in the transference of electron/ion/materials between the materials surface, creating an electric potential difference after their separation. By cyclically contacting and separating materials with oppositely charged surfaces, electrons are driven to flow through the external load, generating a continous output. To optimize the output performance of TENG, the morphology of the surfaces of the triboelectric materials must be modified.

Since the goal of this project is to build a prototype of a triboelectric device, the test system, which helped study the characteristic of the available triboelectric materials, was the first to be developed. With this test system it was also possible to verify that the best results are obtained when employing micro- and nano- texturized materials. For the texturized materials, we obtained a noticeable voltage increase of around 100.0% for both textured samples by using two different methods: Nanoporous Aluminium Templates and Micromachined Silicon Molds. After choosing the best tribo pair material, it was possible to carry out the construction of a prototype which allows harvesting energy from the contact between triboelectric materials, as a result of magnetic coupling between a ferromagnetic ball and a magnetic tape. For this device, the average value open-circuit voltage was $\simeq 4.2\ V$, and for the short-circuit current was $\sim 6.3\ \mu A$, and the maximum power output value was $17.7\ \mu W$ (or $0.04\ W/m^2$). This whole project contributes to the development and optimization of triboelectric generators in the future to come.

Contents

Acknowledgements iii

Resumo v

Abstract vii

List of Figures xi

List of Tables xiii

Abbreviations xv

Physical Constants xvii

Symbols xix

1 Introduction 1
- 1.1 Motivation . . . 1
- 1.2 Aim and Objectives . . . 2
- 1.3 Thesis Organization . . . 2

2 Triboelectric Nanogenerators 5
- 2.1 Fundamentals of Tribology . . . 5
  - 2.1.1 Theoretical Background . . . 6
    - 2.1.1.1 Electron transfer mechanism . . . 7
    - 2.1.1.2 Ion transfer mechanism . . . 8
    - 2.1.1.3 Material transfer mechanism . . . 8
    - 2.1.1.4 Mechano-chemical transfer mechanism . . . 8
  - 2.1.2 Nanotribology . . . 8
- 2.2 Nanogenerators: Energy Harvesting . . . 9
- 2.3 Triboelectric Nanogenerators . . . 11
  - 2.3.1 Basics of triboelectric nanogenerators . . . 12
  - 2.3.2 Fundamental operation modes . . . 14
    - 2.3.2.1 Vertical Contact-Separation Mode (VCTENG) . . . 14
    - 2.3.2.2 Lateral Sliding Mode (LSTENG) . . . 16
    - 2.3.2.3 Single-Electrode Mode (SETENG) . . . 19
    - 2.3.2.4 Freestanding triboelectric-layer mode (FTENG) . . . 20
- 2.4 Architecturing micro/nano-surfaces . . . 21
- 2.5 Prototypes: State of the Art . . . 22

3 Fabrication, Characterization and Testing of Triboelectric Materials 27
3.1 High-Performance Materials Aspects . . . 27
3.2 Experimental Techniques . . . 28
3.2.1 Spin-Coating Deposition . . . 28
3.2.2 Scanning Electron Microscopy - Energy-Dispersive X-ray Spectroscopy . 30
3.3 Surface Texturizing . . . 30
3.3.1 Nanoporous Aluminium Templates . . . 31
3.3.2 Micromachined Silicon Molds . . . 32
3.4 Testing System . . . 33
3.4.1 Experimental Details . . . 34
3.4.2 Servo Control . . . 36
3.4.3 Experimental Results . . . 36
3.5 Summary . . . 39

4 Automated Data Acquisition 41
4.1 Testing System Acquisition . . . 41
4.2 Output Power Acquisition . . . 42
4.2.1 LabView Interface for Arduino Uno . . . 42
4.2.2 Resistor Control and Oscilloscope Data Acquisiton . . . 43

5 Triboelectric-based device: harvesting energy from the environment 45
5.1 Experimental Details . . . 46
5.1.1 Device Design and Development . . . 46
5.1.2 Materials . . . 48
5.1.2.1 Construction materials . . . 48
5.1.2.2 Triboelectric materials . . . 49
5.1.3 Set-up and Measurements . . . 49
5.2 Experimental Results . . . 51
5.2.1 Open-Circuit Voltage and Short-Circuit Current . . . 51
5.2.2 Output Power . . . 54
5.3 Summary . . . 56

6 Conclusions and Future Directions 59
6.1 Conclusions . . . 59
6.2 Future Directions . . . 60

A Arduino Servo Program 67

B LabVIEW Interface 69

List of Figures

2.1 Triboelectric series . . . 6
2.2 Different working principles of nanogenerators . . . 9
2.3 Triboelectric generator . . . 11
2.4 The capacitive behavior of the TENG . . . 12
2.5 Vertical contact-separation mode-based TENG . . . 15
2.6 Lateral sliding mode-based TENG . . . 17
2.7 Rotating TENG . . . 18
2.8 Comparison between the TENGs of lateral sliding mode and the vertical contact-separation mode . . . 18
2.9 Single-electrode mode-based TENG . . . 19
2.10 Freestanding mode-based TENG . . . 21
2.11 Prototypes based on harvesting vibration energy . . . 23
2.12 Prototypes based on harvesting energy from human body motion . . . 24
2.13 Self-powered active chemical/environmental sensors . . . 25
2.14 Summary on the progress made in the output power density of a TENG . . . 25

3.1 Spin-coating deposition process . . . 28
3.2 The influence of speed and time on thickness in the spin-coating process . . . 29
3.3 Laurell WS-650S spinner. Oven for curing PDMS . . . 29
3.4 Anodization process . . . 31
3.5 SEM images of nanoporous aluminium templates . . . 32
3.6 Micromachined silicon molds. Textured PDMS film having patterned the pyramids. 33
3.7 SEM images of PDMS pyramids resulting from Silicon Mold . . . 33
3.8 Scheme of the testing system . . . 34
3.9 The final version of the testing system . . . 35
3.10 Experimental set-up of the testing system . . . 35
3.11 Results of the testing system for both the mean output voltage and the maximum output voltage peak of several materials. . . . 37
3.12 Output voltage of PDMS thin films with non-structured and structured (pyramid and aluminium templates) surfaces . . . 38

4.1 LabVIEW Program used in the testing system . . . 42
4.2 LabVIEW program responsible for initializing Arduino . . . 43
4.3 LabVIEW event case corresponding to one relay . . . 43
4.4 LabVIEW frontpanel for oscilloscope data acquisition and relays control . . . 44

5.1 Sketch of the triboelectric device . . . 46
5.2 Elements of the prototype device . . . 47
5.3 Final configuration of the prototype and respective details . . . 48
5.4 Experimental set-up of the triboelectric device . . . 50
5.5 Open-circuit voltage peaks for four distances between the ferromagnetic ball and the magnetic tape . . . 52

5.6 The dependence of open-circuit voltage with the four distances between the ferromagnetic ball and the magnetic tape. Magnification of a peak voltage from the d_3 distance 53
5.7 Short-circuit current peaks for four distances between the ferromagnetic ball and the magnetic tape 53
5.8 The dependence the output voltage and current on the external loading resistors 55
5.9 The dependence of the output power on the external loading resistors 56

B.1 Initialize LabView interface for Arduino and for Texmaker oscilloscope 69
B.2 Main cycle and closing LabVIEW program 70
B.3 Different event cases available 71

List of Tables

3.1 Comparasion of V_{OC} and $< V_{OC} >$ for non-structured, micro-structured and nano-structured PDMS films. 38

5.1 Mean short-circuit output currents for four distances between the ferromagnetic ball and the magnetic tape. 54

Abbreviations

UP	**U**niversidade do **P**orto
CEMUP	**C**entro de **M**ateriais da **UP**
IFIMUP-IN	**I**nstituto de **F**ísica de **M**ateriais da **UP** - **I**nstituto **N**anociência e Nanotecnologia
INESC-MN	**I**nstituto **E**ngenharia de **S**istemas e **C**omputadores - **M**icrosistemas e **N**anotecnologias
AFM	**A**tomic **F**orce **M**icroscopy
FEP	**F**luorinated **E**thylene **P**ropylene
IDE	**I**ntegrated **D**evelopment **E**nvironment
ITO	**I**ndium **T**in **O**xide
PDMS	**P**oly(**d**i**m**ethyl**s**iloxane)
PMMA	**P**oly(**m**ethyl**m**eth**a**crylate)
PTFE	**P**oly(**t**etra**f**luoro**e**thylene)
PVC	**P**oly**v**inyl **C**hloride
SEM	**S**canning **E**lectron **M**icroscopy
STM	**S**canning **T**unneling **M**icroscope
TENG	**T**ribo**e**lectric **N**ano**g**enerators
USB	**U**niversal **S**erial **B**us
VISA	**V**irtual **I**nstrument **S**oftware **A**rchitecture

Physical Constants

Electrical Vacuum Permitivity	ε_0	$=$	8.854×10^{-12} Fm^{-1}

Symbols

V	Voltage	V
Q	Charge	C
x, d	Distance	m
C	Capacitance	F
R	Resistance	Ω
I	Current	A
P	Power	W (J s^{-1})
σ	Charge density	C m^{-2}
ε_r	Relative dielectric constant	Dimensionless

Para os meus pais
e para o meu irmão.

Chapter 1

Introduction

1.1 Motivation

Nowadays, the search for clean and renewable alternative energy resources is one of the most urgent challenges to the sustainable development of human civilization. This is caused by the depletion of our natural resources and degradation of our environment that are leading us closer to an energy crisis. On a larger scale, alternative energy resources such as solar, geothermal, biomass and wind are being explored to reduce the consumption or even replace the most common energy resources such as coal, natural gas and nuclear. On the other hand, on a much smaller scale, charging technology is desperately needed for more independent and sustainable implantable biosensors, nanorobotics, remote and mobile environmental sensors, homeland security and even portable/wearable personal electronics. In general, the size of the battery is a huge limitation to these systems since it is much larger than the size of the desirable nanodevices. One of the goals for nanotechnology is to build self-powered nanosystems that exhibit ultrasmall size, supersensitivity, extraordinary multi-functionality and extremely low power consumption. As a result, energy harvested from the environment would be sufficient to power a large number of systems in the near future [1].

There is a large amount of types of mechanical energy in our living environment that can be harvested, such as our own body movements, wave motion, mechanical vibrations, dissipated heat and blood flow. Nanogenerators are a new technology capable of converting this energy into electrical energy. Specifically, the triboelectric nanogenerators were invented based on the triboelectric effect, which is a universally known phenomena, although generally regarded as undesirable in electronic systems. This new type of nanogenerator brings together high

performance, efficiency, versatility, and scalability. Since the theory of contact electrification remains poorly understood, and the devices are not yet suitable for energy harvesting at a large scale, it is in our best interest to develop and performing a triboelectric nanogenerator that harvest energy from wave motion.

1.2 Aim and Objectives

The aim of this dissertation is to cover a wide range of domains related to tribology, speciffically the triboelectric-based nanogenerators. We will explore in depth this technology going from the theoretical aspects to manufacturing processes.

To accomplish this, the following objectives were defined:

- To study the triboelectric materials available and optimize them to recovere the friction energy between their surfaces;
- Triboelectric nanomaterials manufacture and characterization of it's morphological, cristallographic and structural properties;
- Analyze and improve the triboelectric response of these materials when subjected to an external stimuli, through a study of their morphology and structure;
- Employ triboelectric structures to develop a prototype capable of harvesting energy from wave motion.

1.3 Thesis Organization

This document starts with an overview of the domain of triboelectric nanogenerators (Chapter 2), extending from the intrinsic Physics behind the technology to the optimization of the triboelectric materials involved. Triboelectric nanogenerators are based on the contact electrification effect and electrostatic induction, i.e. the triboelectric effect, which is a universally known but still somewhat mysterious phenomenon. Additionally, some of the most relevant applications of this emerging nanotechnology are presented.

Following this overview, in Chapter 3, we will discusse the importance of choosing the appropriate materials when developing a triboelectric nanogenerator, especially the effect of

different surface morphologies of these materials on the nanogenerator performance. The experimental techniques used to shape and characterize these will be discussed. Lastly, a thorough description will be made of the development of a reliable and reproducible testing system in order to rapidly infer the potentialities of the fabricated materials and test their aplicability as triboelectric nanogenerators.

In Chapter 4 we will describe the development of the software to acquire and transmits data directly to the computer, used to measure the electrical outputs of the triboelectric materials and the planned subsequent device.

Afterwards, in Chapter 5, special attention is given to the development of a triboelectric-based device. This prototype harvests energy from the contact between triboelectric materials that move as a result of magnetic force between a ferromagnetic ball and a magnetic tape. All the fabrication steps and the testing results are detailed, culminating in a detailed characterization of the device, including not only its complete performance, in relation to its electrical outputs, but also the physical explanation behind this phenomenon.

Finally, after summarizing the presented information, it is provided some of potential further improvements (Chapter 6).

Chapter 2

Triboelectric Nanogenerators

2.1 Fundamentals of Tribology

The word tribology is derived from the Greek word *tribos*, meaning rubbing. Tribology is defined as the science and technology of surfaces interacting in relative motion [2] and is one of the oldest areas of scientific study. It originated more than 2500 years ago when Thales of Miletus carried out experiments showing that rubbing amber against wool leads to electrostatic charging or, as is nowadays called, the triboelectric effect [3].

An everyday example of this phenomenon, is that of someone sliding out of their car seat in a sunny day and touching the door metal handle to get out. All of us have a first hand experience on the small electric shocks that often occur at those moments. These are caused by the fact that the skin is a bad electric conductor, which causes static electricity to be generated due to the contact and separation between the skin and the seat. When we then come into contact with a good electrical conductor (the metal handle) a shock occurs, rapidly discharging all the stored electricity, bringing both to the same electric potential. The triboelectric effect, although quite intuitive and easy to reproduce, is still one the least understood phenomenon of materials charging.

In 1757, Johan Carl Wilcke published an influential study on static charges, including the first triboelectric series [4, 5], which organizes materials according to their ability to gain or lose electrons (Figure 2.1). The triboelectic series is a loose ranking to classify materials according to their polarity when triboelectrically charged. The ranking of a material on this scale can fluctuate, since it depends on several factors such as surface roughness, force of contact,

charge backflow, etc. All these variables add to the difficulty of understanding the tribocharging mechanism makes the triboelectric series a relative comparison between materials, and not a strictly quantitative qualification.

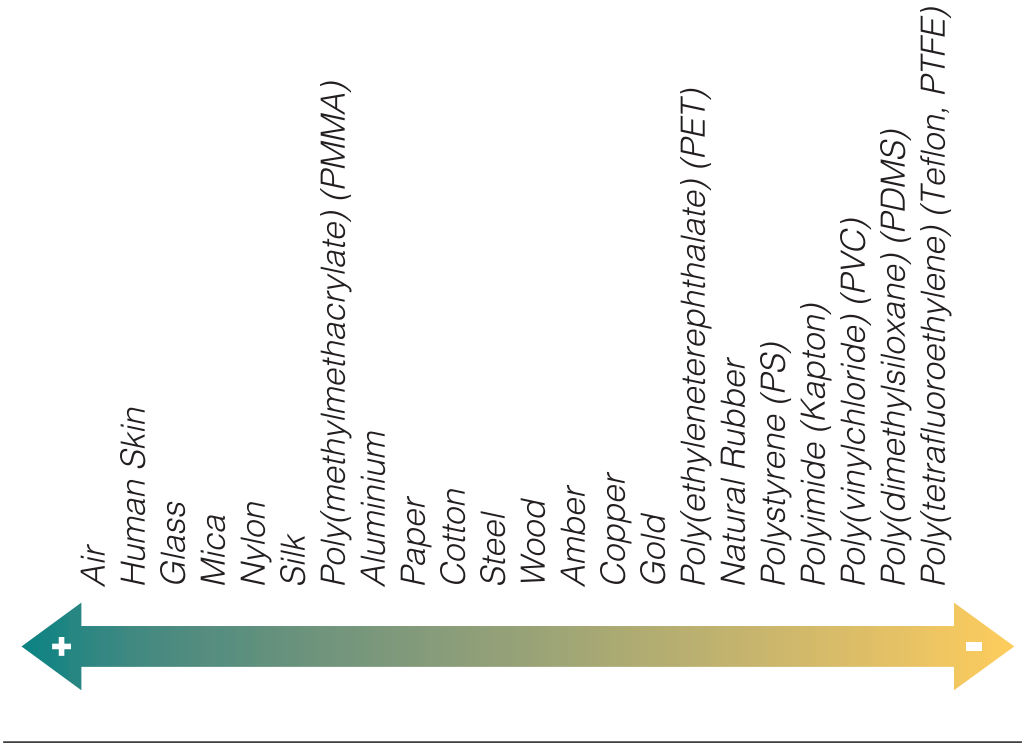


Figure 2.1: Triboelectric series (based on [6–8])

Since the 1800s, tribology has been important in numerous industrial applications having relative motion, such as railroads, automobiles, aircraft, and the manufacturing of electronic components [9]. Much more recently, in the 1990s, new areas of tribology have emerged, including nanotribology, biotribology, and green tribology. These interdisciplinary areas study the friction, wear and lubrication at the nanoscale [including atomic force microscopy (AFM) and micro/nanoelectromechanical systems (MEMS/NEMS)].

2.1.1 Theoretical Background

Despite the fact that contact electrification is a well known phenomenon even to a layman, it is rather surprising that a comprehensive understanding of its mechanisms are still shrouded in mystery. For example, it is still not known which kind of particle is responsible for carrying charge from one surface to the other in processes that involve insulators. This is not the case when discussing conductors, since in this case the process is quite simple. When two metal surfaces come into contact with each other, electrons are transferred from the material with the

lower Fermi level, which is the energy necessary to remove an electron from its surface, to the surface with the highest Fermi level. The amount of charge transferred is then simply based on the difference in these two work functions.

When two surfaces are brought into contact some force is generally necessary to separate them. In this case, the measured forces of adhesion are often attributed to van der Waals forces. Later on, it was shown that charge transfer and the resulting Coulomb forces were responsible for most adhesion phenomena. However, it is not clear if these forces are responsible for the adhesion of the interface when it is not previously charged as in the case of insulators [10]. Furthermore, the surface structure changes during the interaction. Fragments of matter may transfer from one surface to another or break away and plunge into the contact region. Another important factor that contributes to such surface structure changes is the interface temperature of the sliding surfaces, that also plays a meaningful role in their tribological performance.

In the following sections, it is described the various mechanisms that have been put forth to explain contact electrification involving insulating materials [11, 12], which includes the transfer of electrons, ions, or pieces of nanoscopic material.

2.1.1.1 Electron transfer mechanism

The electronic structure of an insulator is usually described by a filled valance band and an empty conduction band. Since an electron cannot be transferred to a valence state, because they are all already filled, and it cannot be transferred to a conduction state because these are much higher in energy, electron transfer to an insulator seems impossible.

The electron transfer mechanism tries to explain contact electrification through the existence of defect states in the band gap, which were not considered in the ideal explanation given above. Basically, these defects are said to be occupied by non-equilibrated electrons or by electrons that are not in their lowest energy state. Many experiments have already been carried out that prove the existence of these electrons. It was verified that these non-equilibrated electrons can remain trapped in high energy states for long times, from days to centuries. These are responsible for the finite conductivity of insulators, and also provide means for contact charging to occur. However, the exact nature of these states is unknown, altough electronic calculations have shown that conformational and chemical defects can give rise to such states.

2.1.1.2 Ion transfer mechanism

The ion transfer mechanism explains the special case of insulating materials where ions are present (ionomers or polymers with molecular salts on surface). These types of materials have strongly bounded ions of one charge polarity on their surface balanced by loosely bound counter ions of the other charge polarity. These last ions are transferred to the other surface upon contact, leaving the original surface with a net charge of the strongly bound ions.

Experiments have been carried out [13], in which a polymer doped with ions is contacted with a metal and ions have been detected on the metalic surface. Based on these results, ion transfer has been considered a general mechanism for contact charging, even for materials without mobile ions.

2.1.1.3 Material transfer mechanism

The material transfer mechanism involves 'patches' of one surface, with an area between nanometers and micrometers, being transferred to the other surface during contact. The patch of material is likely to carry charge, since bonds must be broken for this process to take place.

Recent experiments have shown that, not only does material transfer occur when surfaces contact, but that this transfer changes the way that ions adsortion takes place. This means that material transfer can influence electrostatic charging in a more indirect way.

2.1.1.4 Mechano-chemical transfer mechanism

Finally, there is the Mechano-chemical mechanism, which refers to a class of chemical reactions that occur as a result of bond scission caused by material stress. Any contact between material surfaces can generate stress, by causing bonds in the material to break. A broken bond produces pairs of radicals (if the bond scission is homogeneous), or a positive and negative ion pair (if it is heterogeneous). This model suggests that it is the ions and electrons released by these particles that are then transferred between surfaces.

2.1.2 Nanotribology

The main difference between nanotribology and conventional tribology is the effect of surface forces in the determination of the adhesion and friction behavior of the system. The

interest for nanotribology emerged alongside the proliferation of proximity probes, particularly, scanning probe microscopies (Scanning Tunneling Microscope and Atomic Force Microscopy). These allowed systematic investigations to develop a fundamental understanding of interfacial phenomena on a small scale and to study interfacial phenomena in nanostructures, as well as modifying and manipulating them [9].

The study of nanotribology and nanomechanics are invaluable for the integral comprehension of interfacial phenomena in macrostructures, presenting a bond between science and engineering. The most contemporary example of tribology applied to engineering, are the newly developed triboelectric nanogenerators.

2.2 Nanogenerators: Energy Harvesting

There is a large amount of types of mechanical energy in our living environment that can be harvested, such as our own body movements (as in our muscle stretching and contracting), acoustic/ultrasonic waves, mechanical vibrations, dissipated heat and blood flow. Nanogenerators are a new technology capable of converting this energy into electrical energy. They are typically based on thermoelectric, piezoelectric and triboelectric materials (Fig. 2.2).

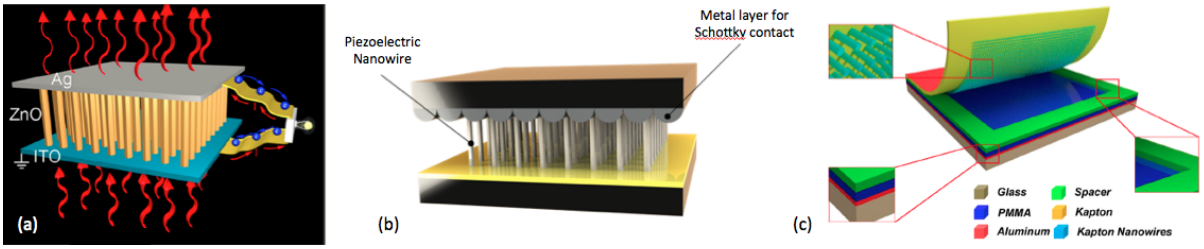


Figure 2.2: Different working principles of nanogenerators: (a) Thermoelectric (from Yang et al. [14]), (b) piezoelectric and (c) triboelectric (from Zhu et al. [15]) nanogenerators.

One of the energy sources that could be harvested is the one that results from heat dissipation. A thermoelectric nanogenerator is an energy harvesting device that converts the external thermal energy into electrical energy by using nano-structured thermoelectric materials, like lead telluride $(PbTe)$, bismuth telluride (Bi_2Te_3), cadmium telluride $(CdTe)$ or silicon-germanium alloys. Usually, harvesting thermoelectric energy relies mainly on the Seebeck effect, which uses a temperature difference between the two ends of the device for driving the diffusion of charge carriers [14]. When a temperature difference is created, the mobile charge carriers in the material migrate to the cold side and leave behind the immobile nuclei

at the hot side, creating a thermoelectric voltage. The voltage measured between the two ends of the junction is proportional to the corresponding temperature difference, with a proportionality constant known as Seebeck coefficient or thermoelectric power. The thermoelectric generators cannot work when the environment temperature is spatially uniform and under a time-dependent temperature fluctuation. This type of nanogenerator has many potential applications, such as wireless sensors, temperature imaging, medical diagnostics, and personal electronic devices.

Piezoelectric materials, such as barium titanate $(BaTiO_3)$, lead titanate $(PbTiO_3)$, lead zirconium titanate $(PZT; Pb[Zr_xTi_{1-x}]O_3)$ or zinc oxide (ZnO), are characterized by a lack of center of symmetry, which results in a piezoelectric effect, by which a mechanical stress/strain can be converted into electrical voltage, and vice versa, owing to the relative displacement of the cations and anions in the crystal. Electrical energy is then obtained from the piezoelectric material and injected into an external circuit directly from two contacts. In the case of piezoelectric nanogenerators, the working principle is the same but with the additional requirement of a Schottky barrier [16]. This allows the device to accumulate all originated electric charges and to release them to an external circuit at a specific position only [17, 18]. The feasible applications of piezoelectric nanogenerators range from self-powered nano/micro devices [19] to transparent and flexible devices [15], smart wearable systems (for example, by integrating them in a pair of shoes to convert the kinetic energy produced by walking), or implantable telemetric energy receivers (implantable device integrated in the nanogenerator that can be operated by receiving external ultrasonic vibration outside the human body, which is converted to electrical energy by the piezoelectric nanostructure). However, the output voltage of this type of nanogenerators is too small (from a few mV to a few V). Thus, a new promising technology appeared, triboelectric nanogenerators, which produce higher output powers, bringing us a broader range of applications.

As stated above, triboelectric materials possess the property of becoming electrically charged upon friction with other triboelectric materials, creating positive or negative charges depending on the materials' tendency to gain or lose electrons, which gives origin to the triboelectric series (Fig. 2.1). Materials with positive charge tendency (such as glass, nylon, silk, PMMA or aluminum) lose electrons when coming into contact with materials of opposite tendency (like amber, polystyrene, silicon or teflon), which gain electrons in the process. The triboelectric nanogenerator (TENG) has been invented as a new technology to harvest this type of mechanical energy, which is based on the contact electrification effect and on electrostatic induction [6].

A triboelectric nanogenerator is composed basically by two triboelectric materials with different polarities, a spacer between them and two metal electrodes. When two triboelectric surfaces (tribo-surfaces) with opposite triboelectric charges (tribo-charges) are periodically contacted and separated, the potential difference between the metal electrodes of the two tribo-surfaces periodically varies, which drives the electrons to flow between the two metal electrodes and generates a continuous output [20]. This new type of nanogenerator brings together high performance, efficiency, versatility, and scalability. Demonstrated applications of this technology include micropatterning [21], powering portable electronics [22], and self-powered sensors [23].

2.3 Triboelectric Nanogenerators

Triboelectric nanogenerators were invented based on the triboelectric effect, which is a universally known phenomena, although generally regarded as undesirable in electronic systems [10, 24]. A traditional triboelectric generator is a mechanical device that produces static electricity or electricity at high voltage by contact charging. The most popular ones are the Wimshurst machine and the Van de Graaff generator, which were invented in 1880 and 1929, respectively (Fig. 2.3). Both machines use the accumulated static charges generated by triboelectrification. These generators are high voltage sources, but there is no current unless there is a discharge [24].

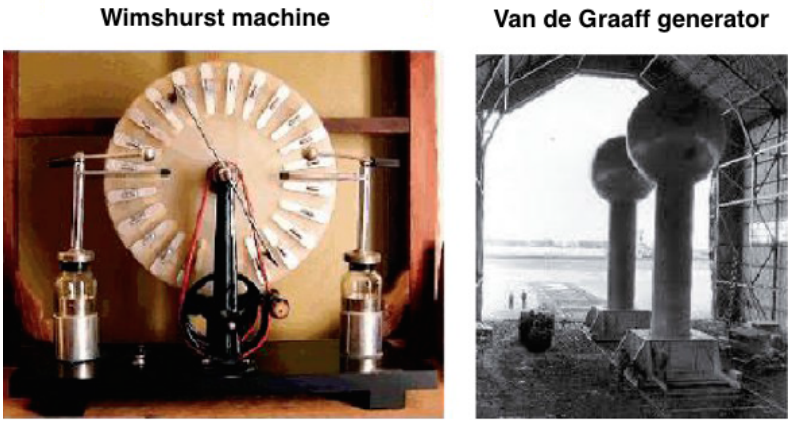


Figure 2.3: Wimshurst machine and Van de Graaff generator, developed a century ago (from Z. L. Wang [25]).

A triboelectric nanogenerator is distinctly different from the traditional Van de Graaff generator in a way that electrostatic induction is introduced so that an output power is obtained.

Wang et al. accidentally discovered the TENG during the development of piezoelectric nanogenerators, in which ZnO nanowires were grown on polymer surfaces. They found that, when these piezoelectric devices were not properly packaged, a voltage of a few volts appeared when the bottom polymer substrate and the top packaging material were brought into contact. Six months of development led to the first paper on the triboelectric generator in 2012. Since then, several tribolectric nanogenerators have been investigated and developed by the same group. One of the first papers was on self-powered pressure sensors based on micropatterned plastic films in May, 2012 [26]. The presented TENG gave an output voltage of up to $18\ V$ at a current density of $0.13\ \mu A/cm^2$ and a peak power density of $23.4\ mW/m^2$. In only a year, the peak power density of TENGs reached $313\ W/m^2$ [22].

2.3.1 Basics of triboelectric nanogenerators

The fundamental working principle of TENGs is a conjugation of contact electrification and electrostatic induction. Contact electrification provides static polarized charges and electrostatic induction is the main mechanism that converts mechanical energy into electricity. A TENG has an inherent capacitive behavior since the most fundamental device based on electrostatics is a capacitor [27].

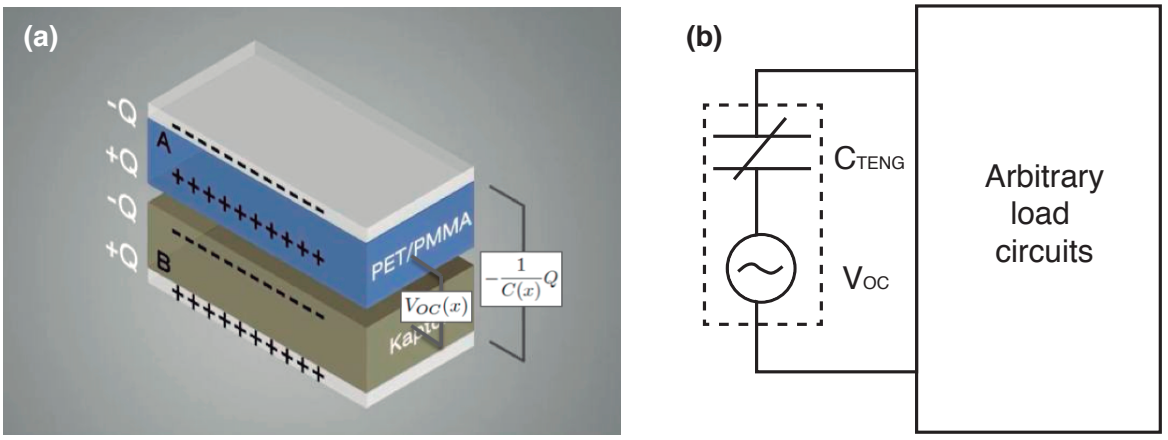


Figure 2.4: (a) Illustration of the capacitive behavior of the TENG (adapted from [28]) and (b) equivalent circuit model of a triboelectric nanogenerator.

The most relevant part of the theory for TENGs is the relationship among three parameters: the output voltage (V), the amount of charge transferred between the electrodes (Q), and the separation distance (x) between the two triboelectric layers; this is the $V - Q - x$ relationship.

After two triboelectric layers get in contact with each other, their contact surfaces will have opposite tribo-charges, as a result of contact electrification. This gives origin to an external current between the two electrodes, as a response to the periodical contact and separation of the two triboelectric layers [see Fig. 2.4(a)]. The polarized triboelectric charges at the contact surface and the transferred charge of each electrode ($-Q$ and $+Q$) contribute to an electrical potential difference between the two electrodes. The first contribution will be the open-circuit (OC) voltage, $V_{OC}(x)$, which is a function of separation distance (x) between the two triboelectric layers, and the second contribution will be $-\frac{Q}{C(x)}$, assuming this structure as a typical capacitor (when no triboelectric charges exist), where C is the capacitance between the two electrodes. Combining the two, the whole equivalent circuit model can be represented by a serial connection of an ideal voltage source and a capacitor, as shown in Fig. 2.4(b). Therefore, due to the electrical potential superposition principle, the total voltage difference between the two electrodes can be given by the previously mentioned $V - Q - x$ relationship:

$$V = -\frac{1}{C(x)}Q + V_{OC}(x). \tag{2.1}$$

At OC conditions, there is no charge transfer, which means that Q is 0. Under short-circuit (SC) conditions ($V = 0$), the transferred charges (Q_{SC}) are related with the electrical potential generated from the polarized triboelectric charges. Hence, the previously equation becomes [29]:

$$Q_{SC} = C(x)V_{OC}(x) \tag{2.2}$$

In the general cases in which a TENG is connected to an arbitrary resistor *R*, the load property can be estimated by combining Eq. (2.1) with Ohm's law:

$$V = IR = R\frac{dQ}{dt} \tag{2.3}$$

Replacing Eq. (2.3) into Eq. (2.1), leads to:

$$R\frac{dQ}{dt} = -\frac{1}{C(x)}Q + V_{OC}(x) \tag{2.4}$$

This is a first-order ordinary differential equation that, by specifying the initial boundary condition [$Q(t = 0)$] for each operation mode, can be numerically calculated. The specific results for two different configurations, contact-separation and single-electrode modes, are explored in detail in Refs. [29–31].

2.3.2 Fundamental operation modes

The TENG has four fundamental operation modes: vertical contact-separation mode, in-plane sliding mode, single electrode mode, and freestanding triboelectric-layer mode. The selection of the different configurations are adjusted depending on the type of applications.

2.3.2.1 Vertical Contact-Separation Mode (VCTENG)

Based on the materials for the triboelectric pairs (tribo-pairs), the vertical contact-separation mode TENG is mainly divided into two categories: dielectric-to-dielectric and conductor-to-dielectric types. The operating principle of the TENG for the case of dielectric-to-dielectric (e.g. PMMA and Kapton; see Fig. 2.1) in contact-separation mode can be described as the periodic change of the potential difference induced by the cycled separation and re-contact of the opposite triboelectric charges on the inner surfaces of the two sheets [21].

In the original state, no charge is generated or induced, with no electric potential difference between the two electrodes (Fig. 2.5-I). When mechanical agitation is applied onto the device to bend or press it, the inner surfaces of the two sheets will get into close contact and then surface charge transfer takes place at the contact area. According to the triboelectric series, electrons are injected from PMMA into Kapton, resulting in net negative charges at the Kapton surface and net positive charges at the PMMA surface (Fig. 2.5-II).

When the deformation is released (Fig. 2.5-III) the two surfaces with opposite charges will separate automatically, so that these opposite triboelectric charges will generate an electric field between them and thus induce a potential difference across the top and bottom electrodes. Defining the electric potential of the bottom electrode (V_{BE}) as zero, the electrical potential of the top electrode (V_{TE}) can be calculated by:

$$V_{TE} = -\frac{\sigma d'}{\epsilon_0}, \tag{2.5}$$

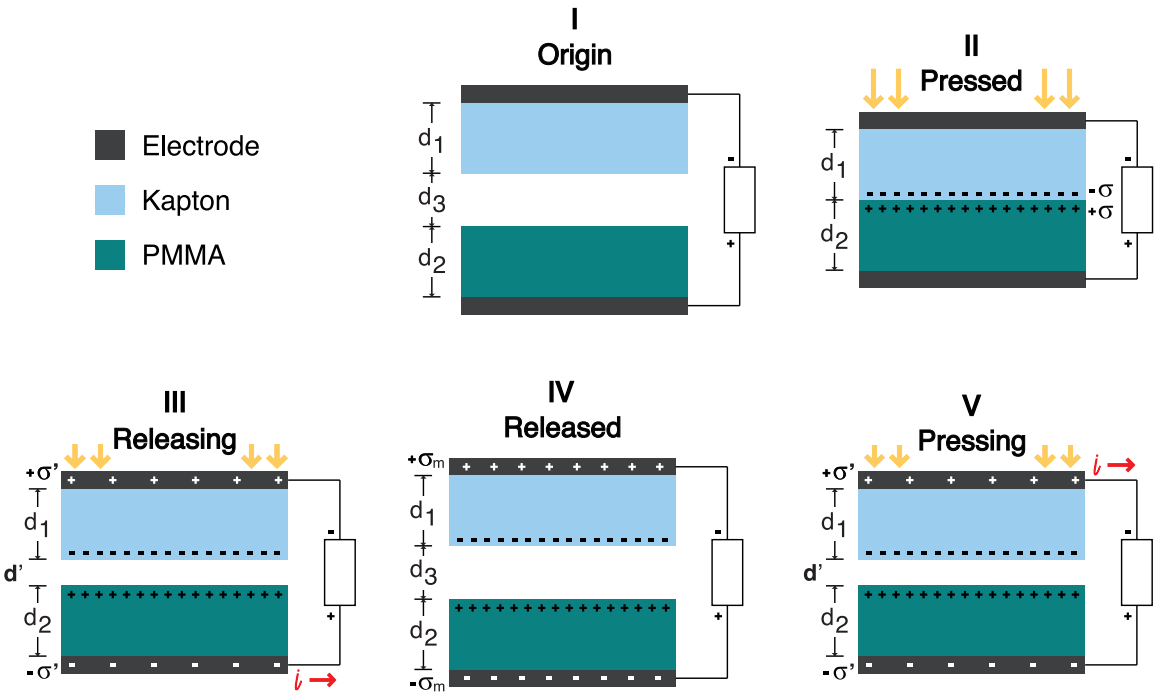


Figure 2.5: Illustration of the operating principle of the TENG for dielectric-to-dielectric in contact-separation mode (adapted from Zhu et al. [21]).

where σ is the triboelectric charge density, ϵ_0 is the vacuum permittivity, and $d^{'}$ is the interlayer distance at a given state [21]. To balance the generated triboelectric potential, the electrons will be driven to flow from the top to the bottom electrode through the external load, resulting in an instantaneous positive current during the releasing process. The induced charge density (σ') when the generator is fully released (Fig. 2.5-IV) is given by:

$$\sigma^{'} = \frac{\sigma d^{'} \epsilon_{rk} \epsilon_{rp}}{d_1 \epsilon_{rp} + d^{'} \epsilon_{rk} \epsilon_{rp} + d_2 \epsilon_{rk}}, \tag{2.6}$$

where ϵ_{rk} and ϵ_{rp} are the relative permittivity of Kapton and PMMA, respectively, and d_1 and d_2 are their thicknesses [21]. The maximum value of $\sigma^{'}$ (σ_m) is obtained by substituting $d^{'}$ (see Fig. 2.5) for d_3 in Eq. (2.6).

When the two sheets are pressed towards each other again (Fig. 2.5-V), the triboelectric-charge-induced potential difference will begin to decrease to zero so that the transferred charges will flow from the bottom electrode back to the top electrode, reducing the amount of induced

charges. This process corresponds to an instantaneous negative current. When the two polymers are in contact again all induced charges are neutralized (Fig. 2.5-II).

2.3.2.2 Lateral Sliding Mode (LSTENG)

Considering the materials to be used as the pair of the triboelectric layers, the sliding-mode TENG, as the VCTENG, also has two types: dielectric-to-dielectric and conductor-to-dielectric.

In Fig. 2.6 is represented a LSTENG for the case of dielectric-to-dielectric (Nylon and PTFE) generator that is designed based on the in-plane sliding between two surfaces [27, 32]. Briefly, the system starts from the position were both electrodes are fully overlaped and in contact with each other (Fig. 2.6-I). Because of the opposite signs of the triboelectricity between Nylon and PTFE, the Nylon surface will accumulate positive charges and the PTFE negative charges with equal density and then generate an electric potential drop across the two electrodes. When one of the surfaces starts to slide (Fig. 2.6-II), a disequilibrium of charges appears (due to the incomplete overlap of the surfaces) and the in-plane charge separation is initiated. These charges will generate an electric field, pointing from the right to the left, almost parallel to the plates, inducing a higher potential at the top electrode. The generated potential difference will drive a current flow from the top electrode to the bottom electrode to generate an electric potential drop that cancels the tribo-charge-induced potential.

Thus, the current flow will continue with the on-going sliding process that keeps increasing the separated charges, until the top plate fully slides out of the bottom plate and the tribo-charged surfaces are entirely separated (Fig. 2.6-III). The measured current should be determined by the rate at which the two plates are being slid apart. Subsequently, when the top plate is reverted to slide backwards (Fig. 2.6-IV), the separated charges begins to get in contact again but no annihilations occurs due to the insulator nature of the polymer materials. This will originate an inverse process, with the charges going from the bottom to the top electrode, in order to keep the electrostatic equilibrium. Once the two plates reach the overlapping position, the charged surfaces get into fully contact, again, returning to the first state (Fig. 2.6-I). In this entire cycle, the processes of sliding outwards and inwards are symmetric, so a pair of symmetric alternating current peaks is expected.

The mechanism of the lateral sliding mode can work in rotation as well. For example, a segmentally patterned diskshaped TENG was designed (Fig. 2.7a) [33], in which a periodic overlapping and separation process of two groups of sectors on the two concentric and closely

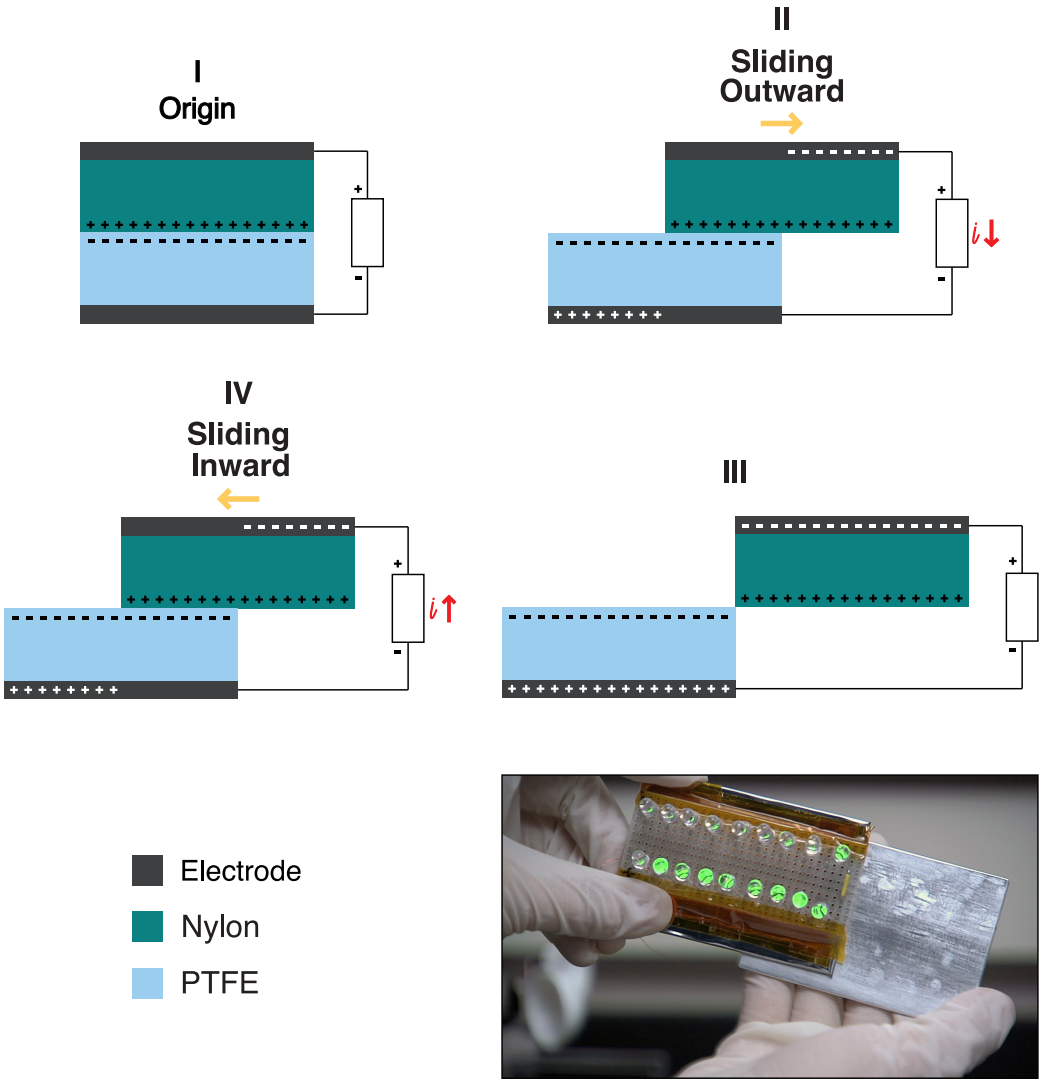


Figure 2.6: Lateral sliding mode: (a) Illustration of the operating principle of the TENG for dielectric-on-dielectric case (from Wang et al. [32]) and (b) and an example of its application (from [28]).

contacted disks is achieved by relative rotation, together with a cylindrical rotating TENG (Fig. 2.7b) [34] based on a core-shell structure that is made of distinctly different triboelectric materials with alternative strip structures on the surface.

Vertical contact-separation versus lateral-sliding modes

The working principle of both the vertical contact-separation and lateral sliding modes is similar. However, the characteristics of the electrical output differ a lot. As shown in the experimental comparison of the TENGs in these two modes (Fig. 2.8), with the same materials and dimensions, the short-circuit current of the TENG, in the lateral sliding mode, has a much

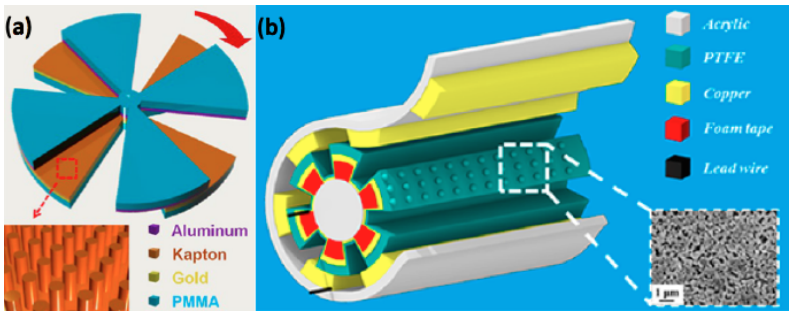


Figure 2.7: Rotating TENG (a) in a segmented disk configuration (from Lin et al. [33]) and (b) in a cylindrical configuration (from Bai et al. [34]).

smaller peak value ($\approx 15\ \mu A$) but a longer pulse (Fig. 2.8a), compared to a much larger peak value ($\approx 240\ \mu A$) but a much shorter pulse of the TENG in the vertical contact-separation mode (Fig. 2.8b).

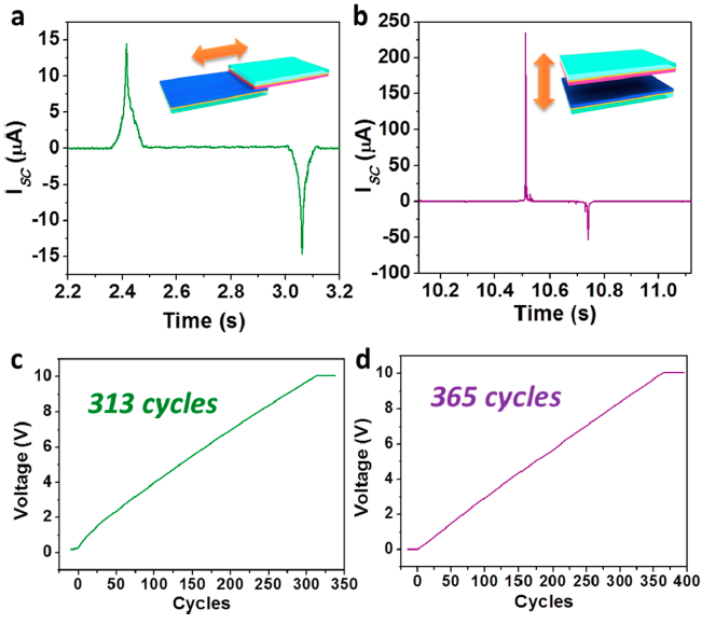


Figure 2.8: Comparison between the TENGs of lateral sliding mode and the vertical contact-separation mode: (a, b) The profiles of the shortcircuit current (I_{SC}) peaks within one cycle for the TENGs of the lateral sliding mode and vertical contact-separation mode, respectively. Two capacitors of $22\ \mu F$ were charged from 0 to $10\ V$ by the TENGs of the two modes, respectively: (c) the TENG of the lateral sliding mode, which takes 313 displacement cycles, and (d) the TENG of the vertical contact-separation mode, which takes 365 displacement cycles (from Wang et al. [32]).

However, it is the total amount of charges, rather than the peak current, that acts as the key factor for the efficiency of charging an energy storage device. In order to charge a capacitor of $22\ \mu F$ from 0 to $10\ V$, the sliding TENG took 313 cycles (Fig. 2.8c), while the vertical-contact TENG took 365 cycles (Fig. 2.8d). So, the TENG in the lateral sliding mode is more efficient

when combined with an energy storage device [32]. It has many other advantages such as structure simplicity, robustness, cost-effectiveness, stable performance and easier fabrication.

2.3.2.3 Single-Electrode Mode (SETENG)

A single-electrode triboelectric nanogenerator is introduced as a more practical and feasible design for some applications such as finger-tip driven triboelectric nanoagenerators [35]. The working principle of the single-electrode TENG is schematically shown in Fig. 2.9. In the original position (Fig. 2.9-I), the surfaces of skin and PDMS fully contact each other, resulting in charge transfer between them. According to the triboelectric series, electrons are injected from the skin to the PDMS. The produced triboelectric charges with opposite polarities are fully balanced/screened, leading to no electron flow in the external circuit.

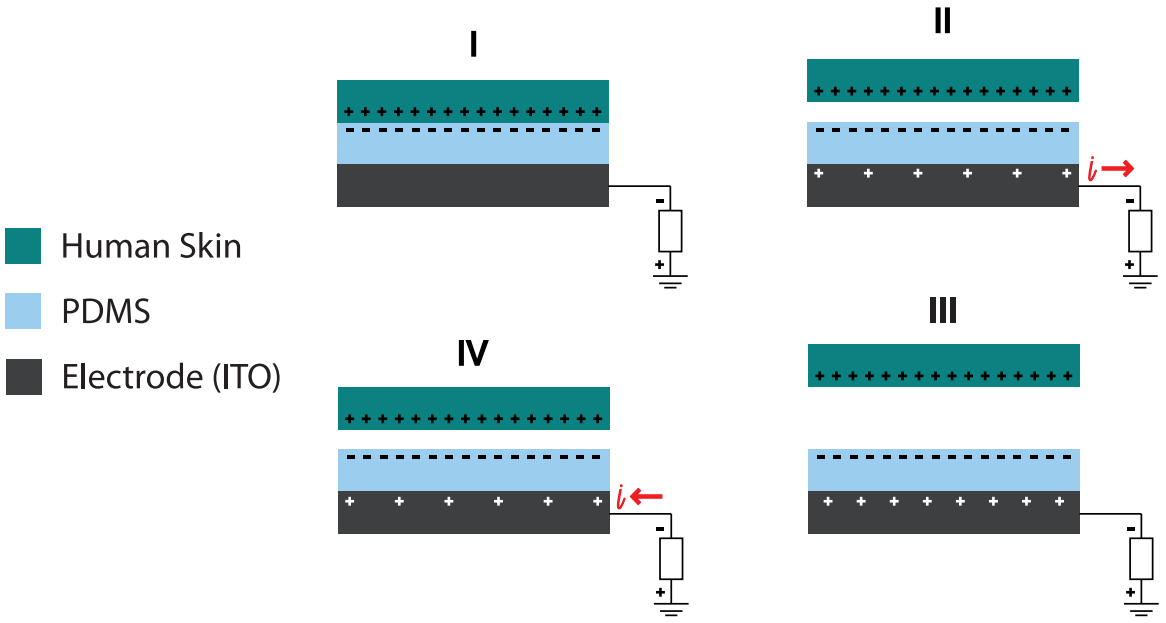


Figure 2.9: Illustration of the operating principle of the TENG for single-electrode mode (from Zhong Lin Wang [6]).

When the PDMS and skin start separating (Fig. 2.9-II), these triboelectric charges cannot be compensated. The negative charges on the surface of the PDMS can induce positive charges on the ITO electrode, driving free electrons to flow from the ITO electrode to the electrical ground. Due to this electrostatic induction process, it is possible to obtain an output voltage/current signal if the separation distance between the touching skin and the bottom PDMS is appreciable comparable to the size of the PDMS film. When negative triboelectric charges on the PDMS are fully screened from the induced positive charges on the ITO electrode by

increasing the separation distance between the PDMS and skin, no output signals can be observed (Fig. 2.9-III). When the skin again approaches the PDMS (Fig. 2.9-IV), the induced positive charges on the ITO electrode decrease and electrons will flow from ground to the ITO electrode until the skin and PDMS fully contact with each other again, resulting in a reversed output voltage/current signal. This is a full cycle of the electricity generation process for the TENG in contact-separation mode. It is also possible to do a mechanism of single-electrode mode based on sliding TENG [36] and even the hybridization of the two modes [37].

2.3.2.4 Freestanding triboelectric-layer mode (FTENG)

The configuration of the existing basic modes of TENGs, the contact mode and the sliding mode, largely limits the TENGs' versatility and applicability for harvesting energy from an arbitrary moving object or a walking human, because the object has to be connected to the entire system by an interconnect. Thus, a new type of design and operation mode was created: a TENG with two stationary electrodes and one freestanding triboelectric layer that moves in between them under the guidance of external mechanical energy [38]. Compared to the above single electrode mode, this new one has no screening effect. Thus, the electrostatically-induced electron transfer can be most effective to reach the same amount of triboelectric charges on the freestanding layer, which achieves higher efficiency.

The freestanding triboelectric-layer mode has two typical configurations. The working principle of the first type of freestanding triboelectric-layer TENG is schematically shown in Fig. 2.10 for the conductor-to-dieletric configuration. Driven by a tangential force, the freestanding FEP layer can slide back and forth between the two electrodes, through which an alternating-current is provided to the load connected between the two electrodes. When the FEP is at a position fully overlapping the first electrode (Fig. 2.10-I), all of the positive charges in the loop will be attracted to the upper surface of the left-hand electrode (LE). Then, when the FEP layer slides towards the right-hand electrode (RE) (Fig. 2.10-II), the positive charges in the loop will flow from the LE to the RE via the load, to screen the local field of the non-mobile negative charges on the dielectric. When the FEP reaches the overlapping position of the RE (Fig. 2.10-III), all of the positive charges will then be driven to the RE. Subsequently, a backward sliding of the FEP layer from the RE to the LE should drive the flow of the positive charges in the same direction, forming a reverse current in the load (Fig. 2.10-IV). This is the full cycle of electricity generation. Compared to the sliding-mode introduced in section 2.3.2.2, the triboelectric layer does not need to maintain the contact with the electrode during sliding, which

means that this mode enables non-contact sliding operation. This advantage largely improves the energy conversion efficiency as well as the long-term stability of the generator by avoiding the direct friction between the two surfaces. Moreover, due to the capability of the non-contact operation, this pair of electrodes can be laminated underneath a dielectric film.

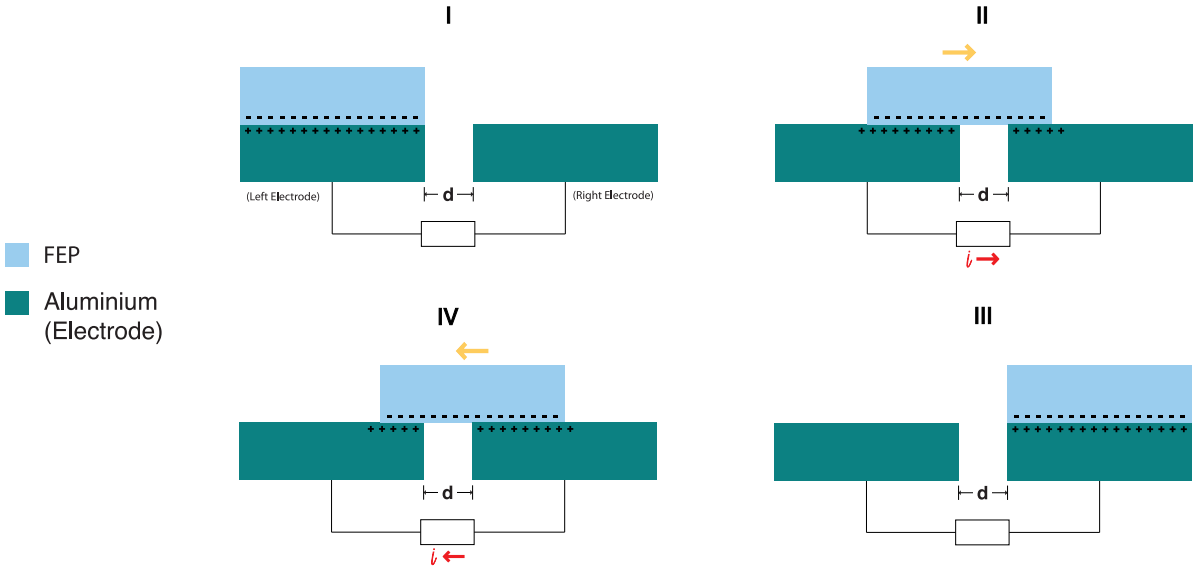


Figure 2.10: Illustration of the operating principle of a conductor-to-dielectric FTENG in the contact sliding mode (adapted from Wang et al. [38]).

In the second type of freestanding triboelectric-layer TENG, the two electrodes are configured face-to-face and the freestanding triboelectric layer oscillates up-and-down in the gap between the electrodes to enable a vertical contact-separation mode [39]. Because of the constant capacitance between the electrodes and the confined electric field, the electricity generation behavior has a linear characteristic, which also enables non-contact operation for the vertical contact mode.

2.4 Architecturing micro/nano-surfaces

Besides all known applications of TENGs, there are still requirements for continuing to improve their output performance, which will need more practical designs and careful optimization of the tribo-pair materials. Changing the tribo-pair materials will strongly influence the output performance due to the change in the tribo-charge density (σ). Thus, in practical TENG designs, optimizing σ is often the only target of material selection [30]. To choose materials that can provide a higher σ, it is necessary to select one material with tendency to lose electrons

and other one with tendency to gain them. This selection is based only on the tribolectric series (Fig. 2.1) since the detailed mechanism of contact electrification is still under investigation. In the triboelectric series the further away two materials are from each other the greater the charge transferred. Materials such as polymers are really promising for the development of nanogenerators due to their flexibility, transparency (in some cases), and their great triboelectric properties, allowing a high efficiency and considerable mechanical resistance, leading to an increase of the durability of the device.

Furthermore, physical techniques can be used to modify the morphology of the surfaces to enhance the contact area and triboelectrification. These techniques include nanostructures, nano-patterns based on pyramids or squares and ion injection which is an effective way to improve σ [26, 40]. However, the bumpy structure that is created on the surface may increase the friction force, and thus reduce the efficiency of the energy conversion of the TENG. In order to maximize the conversion efficiency, the surfaces of the materials can be functionalized chemically using various molecules, nanotubes, nanowires or nanoparticles, which can change the local contact characteristics, improving the triboelectrification. This will require several material studies for later testing and study of the available nanostructures.

Apart from these pure materials, one can also use composites, such as embedded nanoparticles in a polymer matrix [6]. In conjunction with the changes of the surface electrification, it also alters the permittivity of the materials so that they remain efficient for electrostatic induction. Thus, there are plenty of ways to enhance the performance of the TENG, just from the materials standpoint. All this culminates in the large necessity of new studies over practical applications and the actual science of this new technology.

2.5 Prototypes: State of the Art

TENGs, as an emerging nanotechnology to harvest mechanical energy to build self-powered systems, have been used to demonstrate several applications in different areas. In this section we present some of the most relevant applications of TENGs.

A cantilever based on the contact-separation mode TENG is a classical approach for *harvesting vibration energy*, especially for MEMS (Fig. 2.11-I). This TENG, with the assistance of nanowire arrays fabricated onto the surfaces of beryllium copper alloys foils, produces an open-circuit voltage up to 101 V, a short-circuit current of 55.7 μA, with a corresponding peak

power density of $252.3\ mW/m^2$ [41]. A harmonic resonator-based TENG to harvest the energy from an automobile engine, a sofa or a desk, based on the resonance-induced contact separation between two triboelectric materials, is another example of harvesting vibration energy (Fig. 2.11-II). It produces an open-circuit voltage up to $287.4\ V$, a short-circuit current amplitude of $76.8\ \mu A$, and a peak power density of $726.1\ mW/m^2$ [42]. Recently, a three dimensional triboelectric nanogenerator (3D-TENG), which harvests ambient vibration as well, has been designed based on a hybridization mode conjugating the vertical contact-separation mode and the lateral sliding mode (Fig. 2.11-III). Under out-of-plane motion excitation, the 3D-TENG produces an open-circuit voltage up to $123\ V$, a peak short-circuit current density of $30\ mA/m^2$, and a peak power density of $1.35\ W/m^2$. When the 3D-TENG works under in-plane motion excitation, the corresponding electrical outputs are $143\ V$, $32\ mA/m^2$, and $1.45\ W/m^2$, respectively [43]. It has potential applications in environmental/infrastructure monitoring, charging portable electronics, and utility in several internet related technologies.

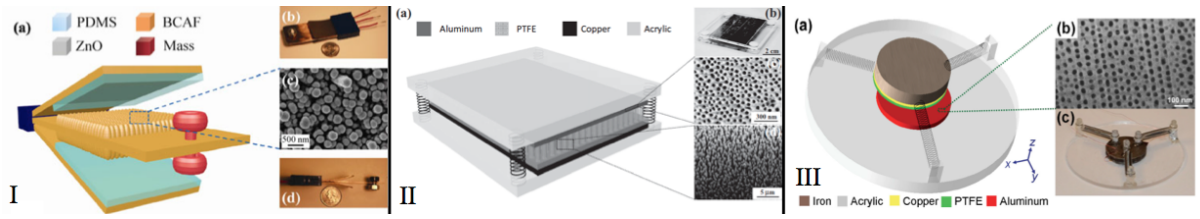


Figure 2.11: Prototypes based on harvesting vibration energy: I - A cantilever based CTENG: (a) Sketch and (b), (d) photographs, and (c) SEM image of Cu film coated ZnO nanowire arrays (from Yang et al. [41]); II - A harmonic resonator based TENG: a) Sketch and (b) a photograph, and (c), (d) SEM image of nanopores on aluminum electrode and PTFE nanowires, respectively (from Chen et al. [42]); III - A 3D-TENG: (a) Sketch, (b) SEM image of nanopores on aluminum electrode, and c) a photograph of the fabricated 3D-TENG (from Yang et al. [43]).

It is possible to make use of the TENG to *harvest energy from the human body motion* which in turn can be used in biomedical applications and self-powered portable electronics. It has been demonstrated that a packaged power generating insole with built-in flexible multilayered triboelectric nanogenerators enables harvesting mechanical pressure during normal walking (Fig. 2.12-I). This TENG relies on the contact-separation mode. Under normal walking, the maximum voltage and current outputs are $220\ V$ and $600\ \mu A$, respectively. To demonstrate the capability of the insole in powering electronics, commercial LED bulbs were directly powered during normal walking [44]. Another example harvesting the energy from human walking, is a rationally designed TENG with integrated rhombic gridding integrated in a backpack (Fig. 2.12-II). With the hybridization of both the contact-separation and sliding electrification modes among nanowire arrays and nanopores fabricated onto the surfaces of two contact plates, this

TENG produces an open-circuit voltage up to $428\ V$ and a short-circuit current density of $36.6\ mA/m^2$, with a peak power density of $30.7\ W/m^2$. The power generated by one unit cell is high enough to simultaneously light more than 40 commercial LEDs, demonstrating its capability as a sustainable power source for mobile electronic [45].

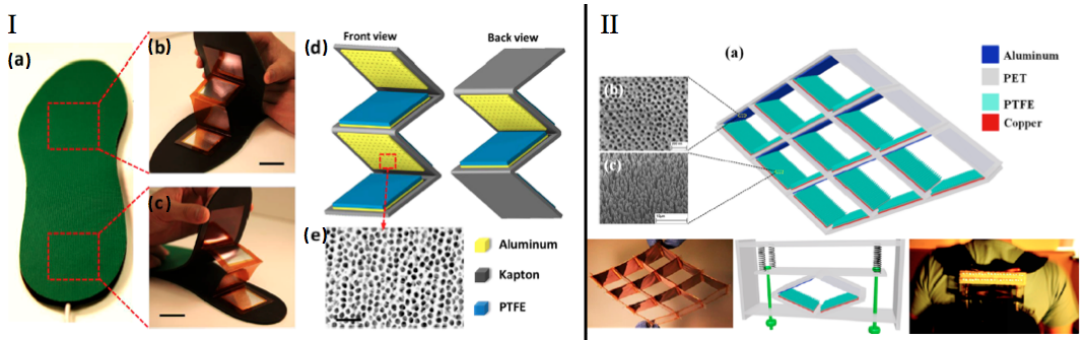


Figure 2.12: Prototypes based on harvesting energy from human body motion: I - Structural design of the power-generating shoe insole based on flexible TENGs: (a), (b), (c) Photographs of a fully packaged power-generating shoe insole, (d) Sketch, and (e) SEM image of nanopores created at the surface of the aluminum foils (from Zhu et al. [44]); II - Integrated rhombic gridding based triboelectric nanogenerator: (a) Sketch, (b) and (c) SEM image of nanopores on aluminum electrode and PTFE nanowires, respectively (from Yang et al. [45]).

In order to increase the output performance of the TENG, it is necessary to select the materials with the largest distance in triboelectric series and changing its surface morphology. So, the output of the TENG depends on the type and concentration of molecules adsorbed on the surface of the triboelectric materials (influencing the triboelectric charge density), which can be used to fabricate *self-powered active chemical/environmental sensors*. An example of this is a TENG used as a sensor for the detection of Hg^{2+}, whose performance depends on the assembly of Au nanoparticles (NPs) onto the metal plate (Fig. 2.13). These assembled Au NPs enlarged the contact area of the two plates, which increased the electrical output of the TENG. On the basis of this structure, the output voltage and current density of the TENGs reached $105\ V$ and $63\ \mu A/cm^2$, respectively, and a peak power of $6.9\ mW/cm^2$ with an effective dimension of $1\ cm^2$ [46].

To summarize, the main progress in the field of TENGs from 2012 to 2013 is depicted in Fig. 2.14 clearly showing a large efficiency improvement that can be used for several types of applications. In fact, nowadays, the main research on TENGs is focused on its packaging in already commercialized products, giving them the ability to have new functionalities. For example, it is worth noticing that recent reports focused on the use of this technology in textiles [47, 48], while other focused in the conjugation of the triboelectric–pyroelectric–piezoelectric effects, by

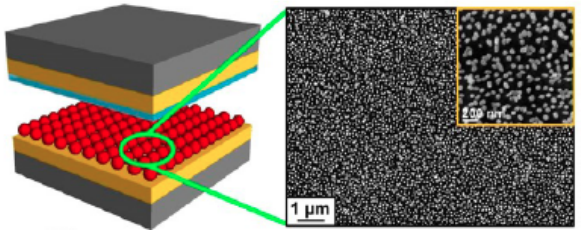


Figure 2.13: Self-powered active chemical/environmental sensors: SEM image of the Au film modified with 56 nm AuNPs (from Lin et al. [46]).

developing a hybrid cell composed of a sliding mode TENG and a pyroelectric–piezoelectric nanogenerator (PPENG), to efficiently harvest energy during friction motion [49].

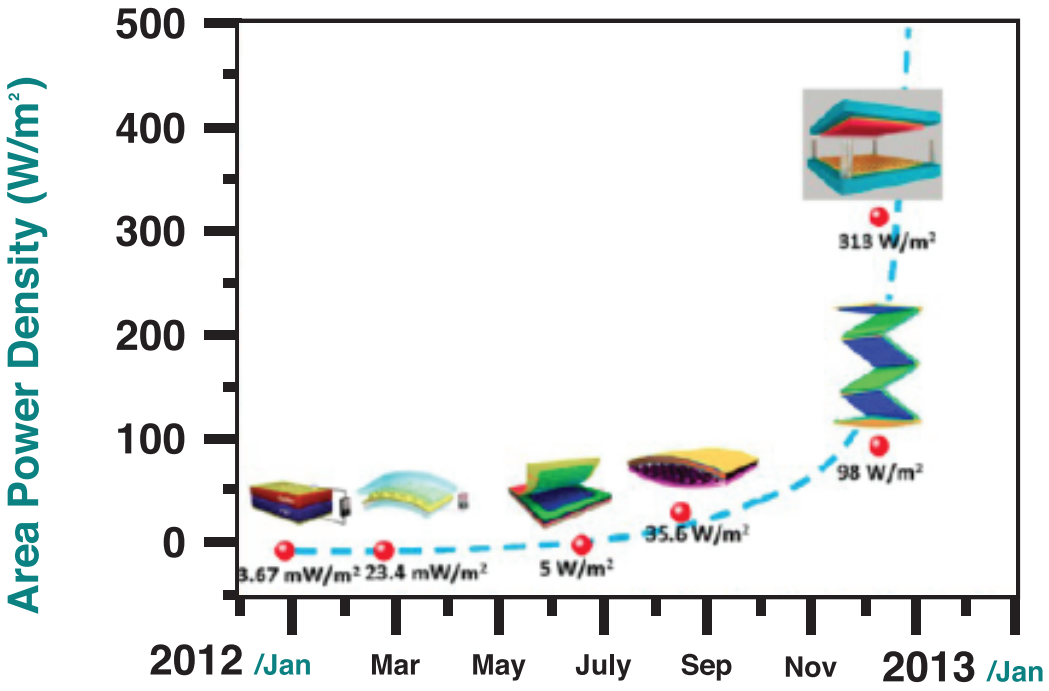


Figure 2.14: Summary on the progress made in the output power density of a TENG in just one year (from Z. L. Wang [8]).

Chapter 3

Fabrication, Characterization and Testing of Triboelectric Materials

In this chapter we will discusse how to choose, fabricate and characterize the appropriate materials to develope triboelectric nanogenerators. There are plenty of choices of materials since almost of them have an inherent triboelectric behaviour. It is in the experimentalist best interest to choose pairs of materials that are far apart from each other in the triboelectric series, in order to enchance the triboelectric effect and the resulting output of a triboelectric generator.

It is thus necessary to evaluate the properties of the available materials. Not only is it important to consider their triboelectric potential, but also other aspects such as their flexibility and durability, the preparation time, the available techniques, and how the consumption of resources in the preparation process. Another meaningful factor to consider is the difficulty of surface texturizing of the said materials. However, after all things considered, one must still have a reliable and reproducible testing system to rapidly infer the potentialities of the fabricated materials and test their aplicability as triboelectric nanogenerators. This thorough materials study will then be employed in building prototypes of electricity generating devices/sensors.

3.1 High-Performance Materials Aspects

To carry out this project, the available triboelectric materials were ordered from the most positive (as in the propensity to lose electrons) to the most negative (propensity to gain electrons) according to the triboelectric series: Nylon, PMMA, Aluminium, Copper, Kapton, PVC,

PDMS, FEP and PTFE. Nylon, PVC, FEP and PTFE are in sheet form; Aluminium, Copper and Kapton are in tape form. Since all these materials are flexible, the design of the device is not as limited, which is an important feature. Regarding their transparency, only Aluminium and Copper, which are mainly used as electrodes, are opaque, while the others are partially (Nylon, Kapton and PTFE) or totally (PMMA, PVC, PDMS and FEP) transparent. One thus expects that the Nylon/PTFE pair will lead to the best results. Most of these materials could thus be used immediately, without needing any sort of preparation/modification, which is a great advantage. However, PMMA and PDMS polymers still needed to be prepared to obtain them in thin film form.

3.2 Experimental Techniques

3.2.1 Spin-Coating Deposition

The spin-coating deposition technique is a common method to produce thin films on flat substrates. Tipically, it is used to deposit photoresist films for the lithographic stages of microelectronic manufacturing processes [50]. An usual process (Fig. 3.1) involves depositing a small volume of a fluid material in the center of a substrate, and then accelerate it to the desired rotation speed. Liquid flows radially, owing to the centrifugal force, and the excess is

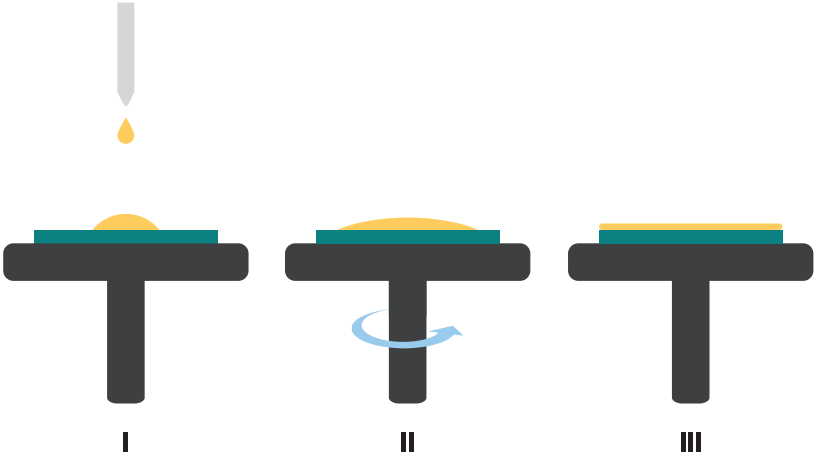


Figure 3.1: Spin-coating deposition process.

expelled to the edge of the substrate spreading and uniformly coating its surface [51]. The spin coating process involves a large number of variables: final film thickness, uniformity and other properties will depend on the nature of the fluid material (viscosity, drying rate, surface

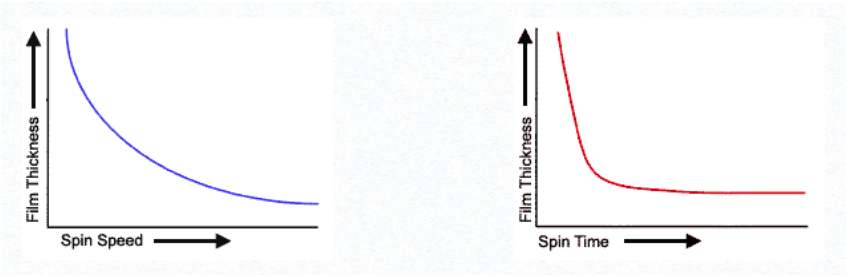


Figure 3.2: The influence of speed and time on thickness in the spin-coating process (from [52]).

tension, etc.) and the parameters chosen for the spin process. In general, higher spin speeds and longer spin times create thinner films (Fig. 3.2).

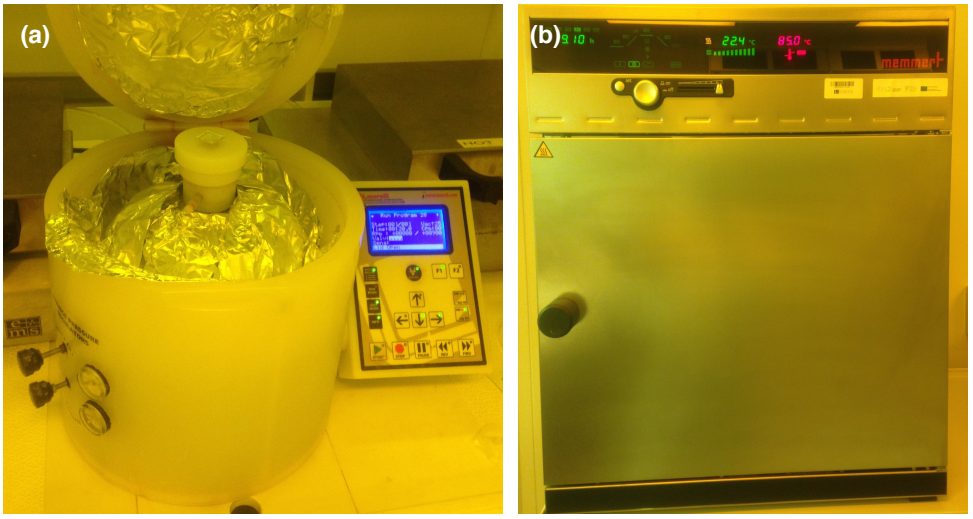


Figure 3.3: (a) Laurell WS-650S spinner; (b) Oven for curing PDMS.

A Laurell WS-650S-6NPP Spinner (CEMUP-MNTEC) [Fig. 3.3(a)] was used to prepare PMMA and PDMS thin films. PMMA is originally in powder form and its preparation involves mixing the powder (12%) with Anisol, resorting to a magnetic agitator for about 4 hours at 50°C. Then it must be uniformly spin-coated over a material that can act as an electrode, and finally placed in a hot plate at 110°C for 1 minute. On the other hand, to prepare PDMS, the liquid PDMS elastomer (with a viscous aspect similar to honey) and cross-linker was mixed in a 10:1 ratio (w/w). It was then degassed, uniformly spin-coated at 500 rpm and then at 900 rpm, for 30 seconds each, and incubated at 80^oC for 2 hours [Fig. 3.3(b)].

3.2.2 Scanning Electron Microscopy - Energy-Dispersive X-ray Spectroscopy

The Scanning Electron Microscope (SEM) is a powerful instrument which permits observation and characterization of heterogeneous organic and inorganic materials and surfaces at a local scale [53]. The primary reason for the SEM's usefulness is the high resolution (better than 1 nm) that can be obtained when bulk objects are examined. Another useful feature is the three-dimensional appearance of the specimen image, that results from the large depth of field, providing a large amount of information about the specimen.

SEM irradiates a finely focused electron beam, taking advantage of their much smaller wavelengths compared to photons, in the area or micro volume to be examined. When the electron beam impinges on a specimen surface some type of signals are produced, such as, secondary electrons, backscattered electrons, Auger electrons, characteristic X-rays, and photons of various energies. These signals are obtained from specific emission volumes within the sample and can be used to examine many characteristics of the sample, like its composition, surface topography, cristallography, etc.

In the SEM the signals of highest interest are usually the secondary and backscattered electrons, since these vary according to differences in surface topography as the electron beam sweeps across the specimen. The secondary electron emission is confined to a volume near the beam's impact area. As a complementary technique, the energy-dispersive X-ray spectroscopy (EDS) analyzes the emitted X-rays and identifies the constituting atomic species of the scanned area.

All the SEM images here presented were obtained with a high resolution FEI Quanta 400FEG scanning electron microscope (CEMUP).

3.3 Surface Texturizing

As mentioned previously, one way to increase the triboelectrification effect is by texturizing the surface of the materials. These materials can be functionalized chemically using various molecules, nanotubes, nanowires or nanoparticles. Surface functionalization can largely change the surface contact area, surface charge transfer density and the surface friction coefficient. The available materials to achieve such texturizing are PMMA and PDMS. Two different

methods were here applied: to use the bottom of anodized alumina templates and micro-machined silicon pyramids as molds to induce nano and micro structures on the polymers surfaces, respectively.

3.3.1 Nanoporous Aluminium Templates

Some metals, like aluminium, are chemically unstable at room temperature when in contact with oxygen, which gives rise to the formation of an oxide in the surface. This superficial oxide layer, designated as alumina layer, is formed spontaneously. However, in order to accelerate the chemical reaction, an electrochemical process called anodization is often applied.

Anodization consists in the application of an electrostatic field [Fig. 3.4(a)], between the aluminium sample (anode) and a metallic mesh (cathode), which promotes the growth of the alumina layer at the metal/oxide interface through electromigration of OH^- and O^{2-} ions, deriving from the ionization of the solution. Simultaneously, the oxide dissolution occures at the oxide/eletrolyte interface, with the incorporation of Al^{3+} on the solution. At the cathode, the H^+

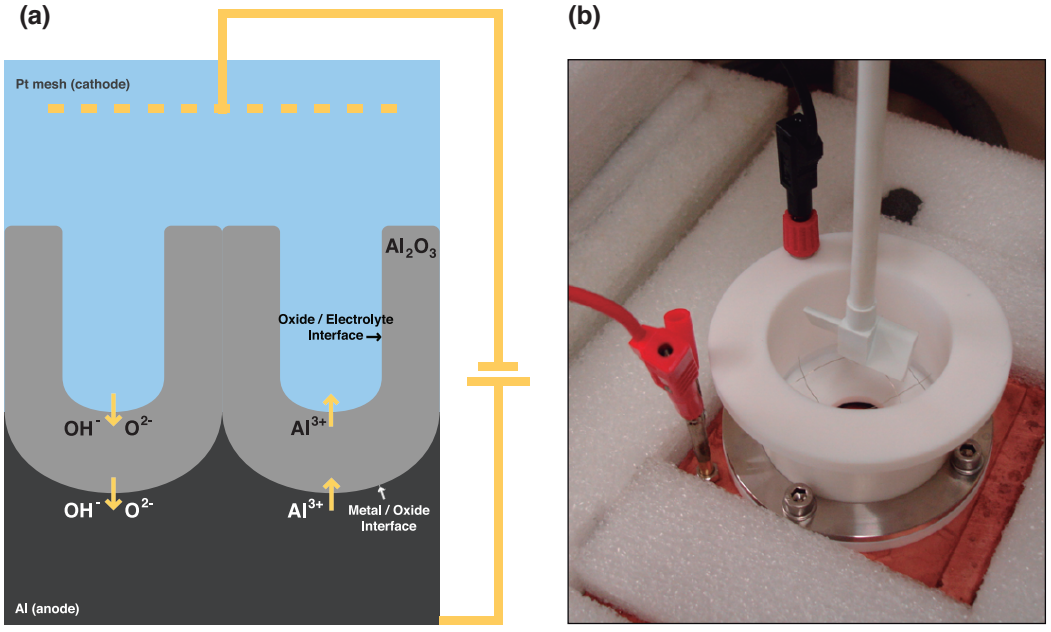


Figure 3.4: Anodization process: (a) eletrochemical processes (adapted from [54]) and (b) experimental setup.

ions absorb electrons coming from the dissociation of the acid which then releases H_2 in its gaseous state. In order to counter the existence of superficial tension in the growing alumina layer, created due to the fact that the alumina volume is significantly larger than the aluminium

one, auto-organized nanopores are formed. The choice of the acid solution to be used in the electrochemical process is crucial, since different acids result in different nanopore diameters. For a better organized structure to be obtained, it is common to perform a two step anodization process [55]: after the first anodization, the resulting alumina is removed and a second anodization takes place afterwards, but this time the nanopores will grow with an improved organization in the hexagonal shaped cavities already present in the aluminium, which resulted from the nanopores created in the previous process. This procedure is mainly used with the purpose of obtaining self-organized alumina templates for the manufacture of nanostructures, such as nanowires or nanotubes.

In the specific case of this study, the objective was to take advantage of the hexagonal cavities resulting from the nanopores created in the first anodization. For this effect, phosphoric acid was used in the anodization process, with an applied potential of 195 V, for 12 hours. The layer of alumina was then removed (for 6 hours) and the chosen material (in this case PDMS) spin coated and annealed on top of the aluminum layer. The aluminium was then detached from the polymer by simply pasting an aluminium tape on the sample and pulling it.

SEM was used to verify the aplicability of this method. As shown in Fig. 3.5, the desired texturization of the PDMS surface was obtained, with an average texture size of $450\ nm$.

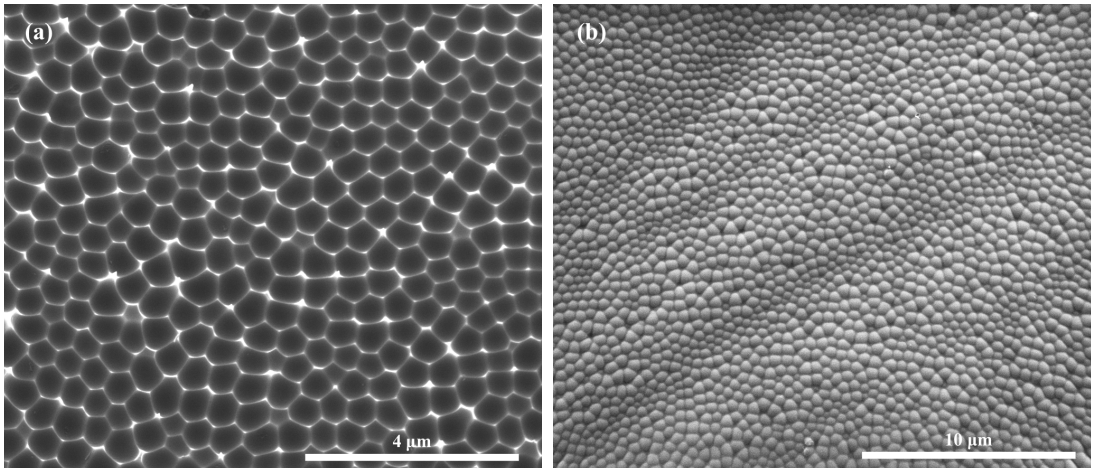


Figure 3.5: SEM images of (a) nanoporous aluminium templates and (b) the respective PDMS texturized top views.

3.3.2 Micromachined Silicon Molds

The second method to make patterned PDMS films was by using a silicon mold provided by INESC-MN, Lisbon (Fig. 3.6). Silicon wafer molds were first fabricated by a traditional

photolithography method, followed by a wet etching process resulting in the formation of recessed pyramids (this pattern leads to the best output voltage of triboelectric nanogenerators [26]). As described above, the liquid PDMS elastomer and cross-linker were mixed, degassed, and uniformly spin-coated on top of the silicon mold. After curing, a uniform PDMS layer was peeled off from the mold, containing the inverse of the original features patterned on the silicon surface.

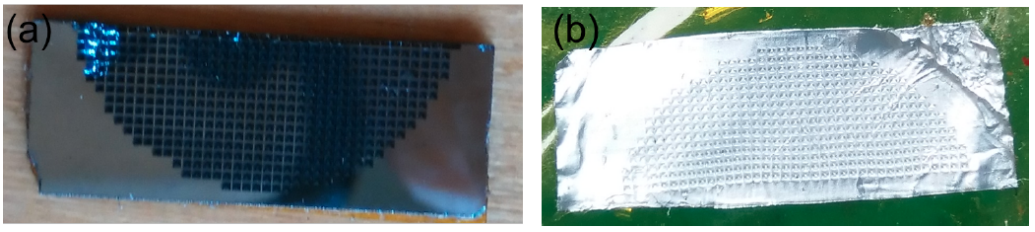


Figure 3.6: (a) Micromachined silicon molds; (b) Textured PDMS film with the patterned pyramids.

High-magnification SEM images (Fig. 3.7) illustrate that the pyramides are regular and remarkably uniform, demonstrating that the followed procedure is an efficient method to obtain textured structures. The length of the base of PDMS pyramides was about $330\ \mu$m.

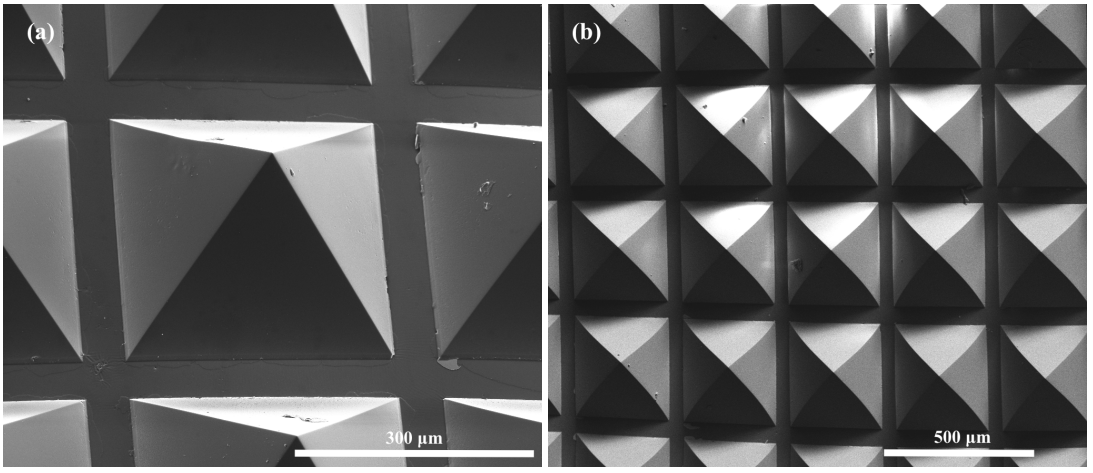


Figure 3.7: SEM images of PDMS pyramids resulting from the Silicon Mold (a) an individual pyramid and (b) an overall image.

3.4 Testing System

With the purpose of studying the best available triboelectric materials, a testing system was designed and assembled. The relative position of these materials in the triboelectric series was verified by evaluating the output potential from the periodic contact-separation of two

triboelectric materials. With the acquired information and considering its other intrinsic characteristics, it was possible to choose the most appropriate pairs of triboelectric materials to use in developing a working prototype.

3.4.1 Experimental Details

Figures 3.8 and 3.9 show a scheme and a photography, respectively, of the testing system used for the aforementioned tests. It consists in a metal plank where two supports with two triboelectric materials, and respective electric contacts, are placed. One of the supports is

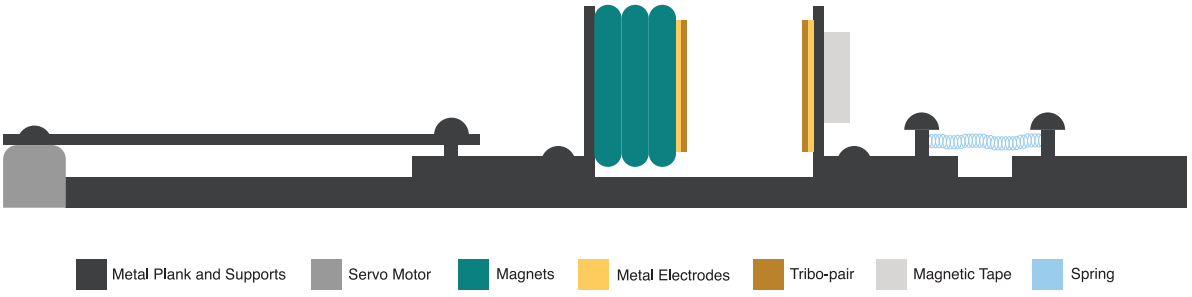


Figure 3.8: Scheme of the testing system.

fixed to a spring and the other (which has a magnet) is secured by a mechanical arm that moves by the action of a rod system rotated by a High Speed Continuous Rotation servo from Parallax Inc. [56], making the support slide back and forth. Each support contains a different triboelectric material and the respective electrode. When the support, attached to the magnet, is close enough to the other, which is fixed to the spring, the magnetic force between them results in the full contact of the pair of triboelectric materials until the spring makes them recover their original position. The servomotor is controlled using an Arduino UNO connected to a personal computer, and the data acquisition is made using a Tektronix TDS 1002C-EDU oscilloscope, which in turn is linked to a computer running a LabVIEW program (Fig. 3.10). The programs responsible for the data acquisition process will be explained in depth in the next chapter.

The testing system was originally projected to test not only conventional materials, but also materials with magnetic properties, particularly composites of polymer (PDMS) and iron oxide nanoparticles. Some problems with these materials emerged later on, such as the non-uniformity of the nanoparticles distribution, due to the limited applicability of the preparation techniques and to the big amount of nanoparticles necessary to be attracted by the magnet

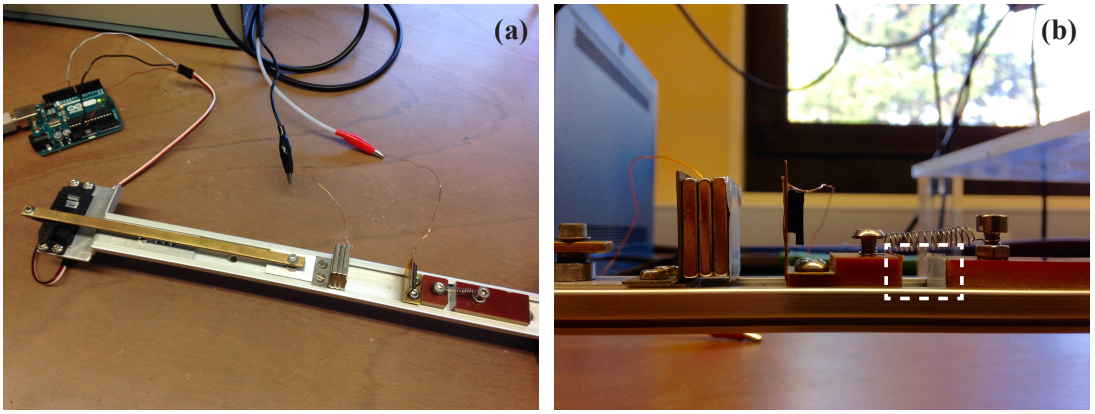


Figure 3.9: The final version of the testing system; the dashed section corresponds to the contact area that harnesses energy from the restorative force of the spring.

integrated in the test system. Although this fact led to the discontinuation of testing in this type of samples, it worked remarkably well for non-magnetic materials and was therefore used in the continuation of this project.

In the second version of the test system, to counterbalance the fact that non-magnetic materials were going to be employed, magnetic tape was attached to the spring support, ensuring the contact between the pair of triboelectric materials (Fig. 3.8).

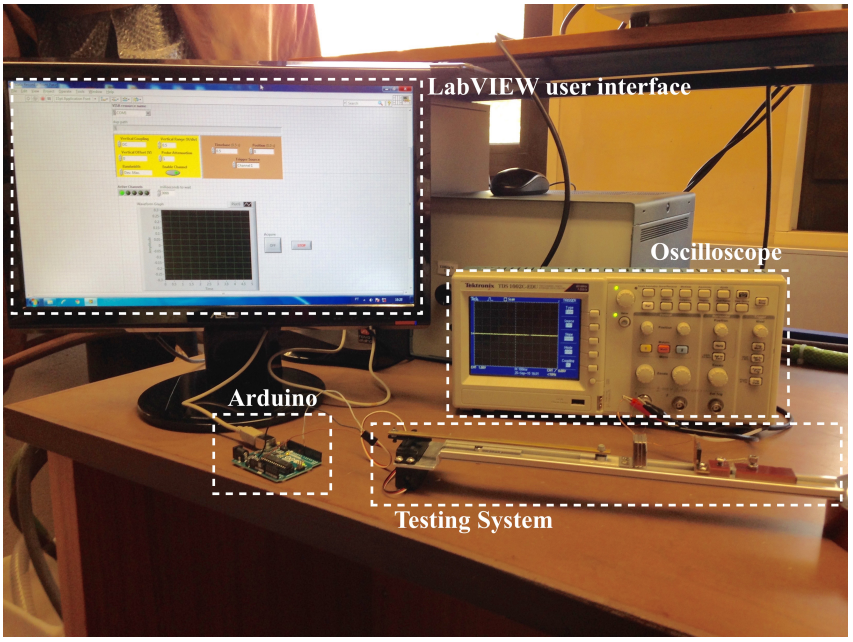


Figure 3.10: Experimental set-up of the testing system.

Lastly, it was noticed that the restoring force from the spring could be beneficial to improve the efficiency of the test system. This configuration is presented in Fig. 3.9(b) (dashed section).

In fact, in the next section, it can be observed that the output voltage obtained using this version increased substantially even though the surface area was decreased to half of that of the original versions.

However, the test system can still be improved. One of the observed problems is the fact that the support (attached to the spring) is deformed after a fair amount of cycles, which results in an incomplete contact between the two materials. One way to solve this issue could be by using a support made from an harder, non-magnetic material.

3.4.2 Servo Control

The program used to control the Arduino UNO, which in turn controls the servomotor, is presented in Appendix A. The Arduino UNO, connected to a computer through an USB port, was programmed with the Arduino Software (IDE), which includes a serial monitor, that allows simple textual data to be sent to and from the board.

The program allows two different servo rotations (clockwise or counterclockwise). The motor operates between the value of 0 to 180. The rotation speed is controlled by the values set on the variable `'val'`, where the interval between 0 and 92 makes the servo rotate clockwise, 94 to 180 makes it rotate counterclockwise and 93 corresponds to the value in which the servo is stationary. The speed of the servo motor is configured in such way that its maximum value is defined as 0, and diminishes until 92, and starts increasing again, but in the other direction, starting at 94 and until the maximum speed is reached at 180.

The values chosen for the execution of these tests, with the servo motor rotating clockwise, were 0, 85, 88, 90; from 0 to 85 the rotation speed is almost unchanged, and starting at 90 the motor does not have enough power to separate the magnet from the other support.

3.4.3 Experimental Results

So that the study of the previously mentioned materials could take place, Nylon, the most positive material available, was the material present in every single pair, which means that the position of the others materials in the triboelectric series was made relatively to Nylon. The size of the samples were roughly the same as that of the supports ($2\ cm^2$) but the effective contact area of the materials were approximately $1.8\ cm^2$. It was possible to control the speed of the motor, through the mentioned Arduino program, allowing the test of four different velocities for

each triboelectric pair: the maximum speed attainable from the motor (0), the lowest (90), that still allowed the support, with the magnet, to be separated from the other support, and two intermediary ones (85 and 88).

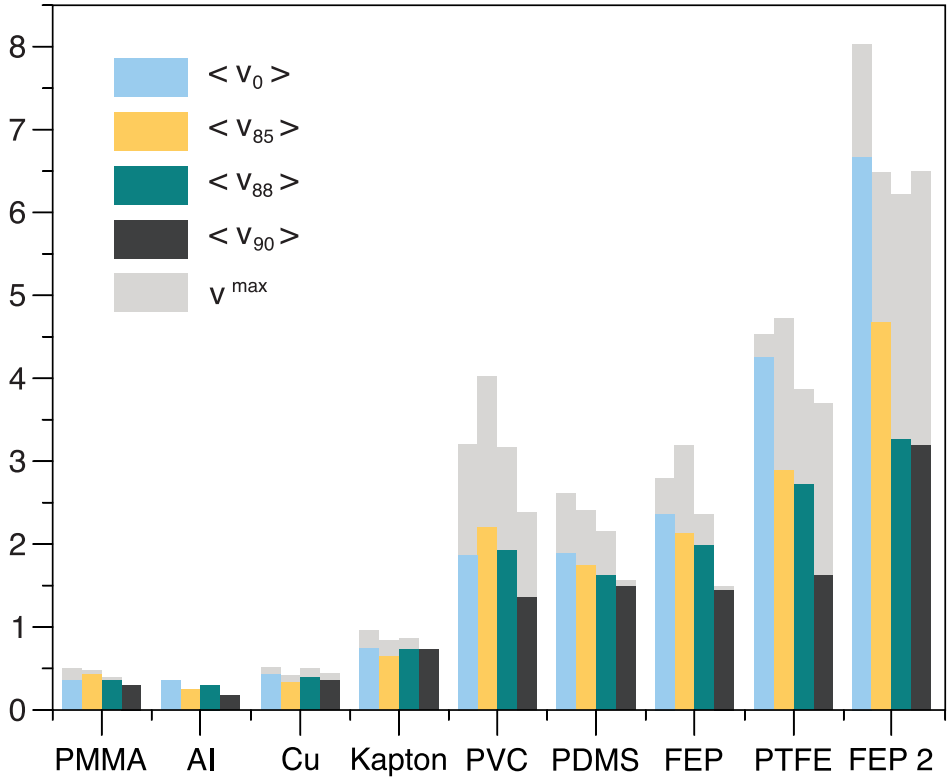


Figure 3.11: Results of the testing system for both the mean output voltage ($< V_x >$) and the maximum output voltage peak (V^{max}) of several materials.

This experimental set-up allowed acquiring data repeatably and reliably. The results acquired (Fig. 3.11), followed the order of the triboelectric series, for any velocity, with the exception of Aluminium and PDMS, whose results are slightly inferior to those of PMMA and PVC, respectively. Since Aluminium was available in sticky tape form, it may have hindered the electron transfer to the electrode. It was verified, in general, that the output diminishes with decreasing velocity, which translates to a smaller impact force between the materials when they are attracted. In other words, the impact force with which the magnet, placed in the support, attracts the magnetic tape in the other support with less speed.

The restorative force of the spring was then harnessed (FEP 2 in Fig. 3.11) only in the final version of the device, since the servo posed some limits in terms of strength. It was verified that even with half the contact area of the original samples, the output increased substantially ($\sim$ 3 x). This was only tested for one material (FEP) since this alteration was made only in

the final phase of the project and, above all, its purpose was only to prove that the triboelectric effect improves considerably with the applied force.

Relatively to the texturized materials, whose contact surface area were $\sim 0.75\ cm^2$, we obtained an evident voltage increase of around 100.0% for the prepared sample using the Nanoporous Aluminium Template as mold and of $\sim$ 111.1% for the sample prepared using the Silicon mold (also relatively to Nylon), as shown in Fig. 3.12 and summarized in Table 3.1. Therefore, with the texturized PDMS, there is an increase of the effective friction area, and thus of the triboelectric effect.

PDMS	$V_{OC_{max}}\ (V)$	$< V_{OC} > (V)$
Non-structured	1.4	$\sim$ 0.9
Micro-pyramids	2.6	$\sim$ 1.8
Nano-structured	2.6	$\sim$ 1.9

Table 3.1: Comparasion of V_{OC} and $< V_{OC} >$ for non-structured, micro-structured and nano-structured PDMS films.

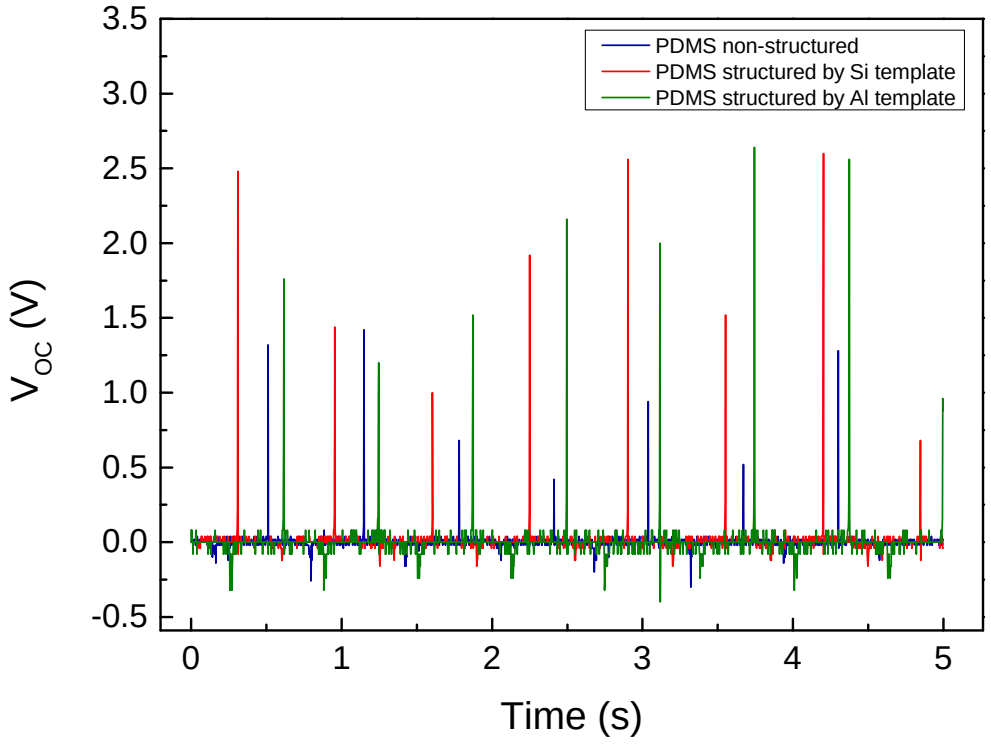


Figure 3.12: Output voltage of PDMS thin films with non-structured and structured surfaces (pyramid and aluminum templates).

3.5 Summary

In summary, the developed testing system allowed verifying that the best triboelectric pair is Nylon and PTFE, the materials available that are placed farther away in the triboelectric series. However, the Aluminium position was not the expected one, but it is also known that the triboelectric series is not fully reproducible, since different experiments lead to different orderings of materials, most likely because of small differences in the material, environment, or the measurement technique used. Another conclusion that was reached was that the increase of the impact force between the pair of materials led to an augmentation of the triboelectric effect.

To texturize the surface, the PDMS was chosen because of its easier preparation and better structural consistency allowing for a more resistent polymer to be obtained. With this in mind, two different methods were applied: Nanoporous Aluminium Templates and Micromachined Silicon Molds. The considerable increase in the electrical output of the structured films over the unstructured films can be attributed to the following factors:

- A surface with more sophisticated structures has a much more effective triboelectric effect and also generates more surface charges during friction;
- The capacitance change in the deformation process is significantly improved due to the presence of air voids and the increase in the effective dielectric constant.

Significant advantage of these techniques include the countless replicas of patterned PDMS films that can be produced from one single mold, and their easy and low-cost manufacture process.

Chapter 4

Automated Data Acquisition

An essential part of this project relied on the development of software that acquires and transmits data directly to the computer. The main objective for these programs was to be employed on the previously described testing system and in the study of the output power of the tribo-pairs, and the planned subsequent device.

4.1 Testing System Acquisition

A Tektronix TDS 1002C-EDU oscilloscope [57] was used to aquire the signal from the tribo-electric effect between the two materials placed in each support of the Testing System. Electric contacts, connected to the electrodes of each tribo-pair, allowed checking the open-circuit output voltage on the oscilloscope (in channel 1). Consequently, it communicates to a computer through an USB port, which allows saving data. For this purpose, the automated measurements and its data acquisition were made through a LabView program, originally developed by the IFIMUP-IN research group, and then adapted for this particular project.

The LabVIEW language was chosen to control the entire experiment due to its great integration with peripherals (Arduino, Oscilloscope, etc.) via the VISA module. It also allows customizable real time data treatment and storage. All this culminates in an easy way to create an accessible user interface.

This interface (Fig. 4.1-a) allows a variety of functions such as: selecting the equipment (VISA module), inserting the files save destination, acquiring and visualizing the characteristics

of the signal received for the oscilloscope. Likewise, it is possible to acquire all required oscilloscope windows by pressing the *Acquire* button. Figure 4.1 also shows the algorithm used to visualize the oscilloscope signal (b) and to convert the acquired data (c) in a '`.txt`' file, for analysis.

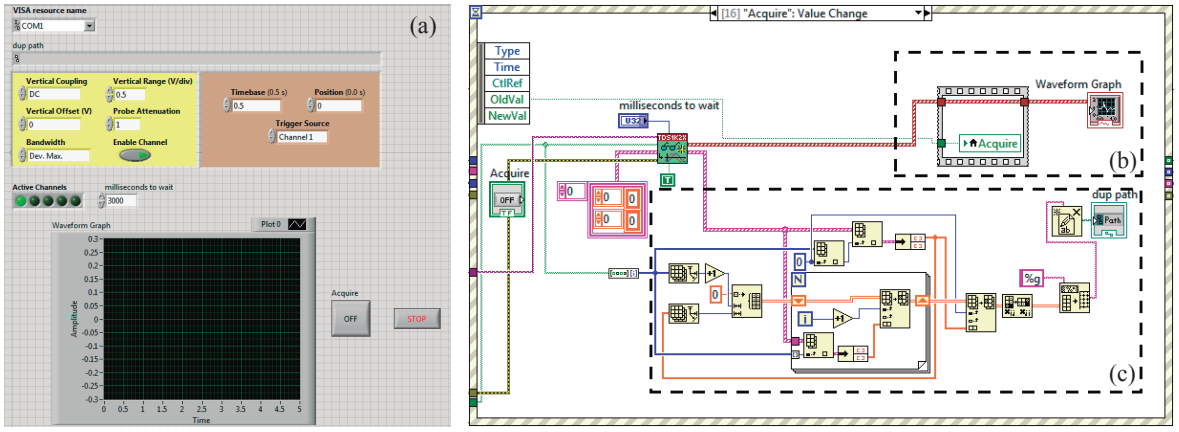


Figure 4.1: LabVIEW program used in the testing system: (a) user interface and respective algorithm that enables (b) the visualization of the oscilloscope signal and (c) the format conversion of the acquired data.

4.2 Output Power Acquisition

With the purpose of further investigating the output power of the tribo-pairs and the planned subsequent device, Cátia Rodrigues, during her Master Thesis, developed a circuit board containing resistors, ranging from $10\ \Omega$ to 10 GΩ, which were used as external loads, following Eq. (2.4). The resistors were connected to relays, so that they could be selected automatically through an Arduino UNO, which in turn, is managed by a LabView program. Measurements of the open-circuit output voltage and short-circuit output current were made for each resistor, in order to calculate the corresponding output power value: $P = VI$. Thus, to carry out this study, the LabView Interface for Arduino UNO was used along with LabView Interface for the Texmaker Oscilloscope.

4.2.1 LabView Interface for Arduino Uno

An external voltage source powers each relay in the circuit board, which are connected to each one of the twelve available digital Arduino pins. In Fig. 4.2 is represented the section of

the program that is responsible for initializing the Arduino, which includes functions that test for errors and set all pins to zero value. This means that every relay is turned off in order to avoid selecting more than one relay simultaneously during the measurements. These are basically switches that can be selected individually through the user interface.

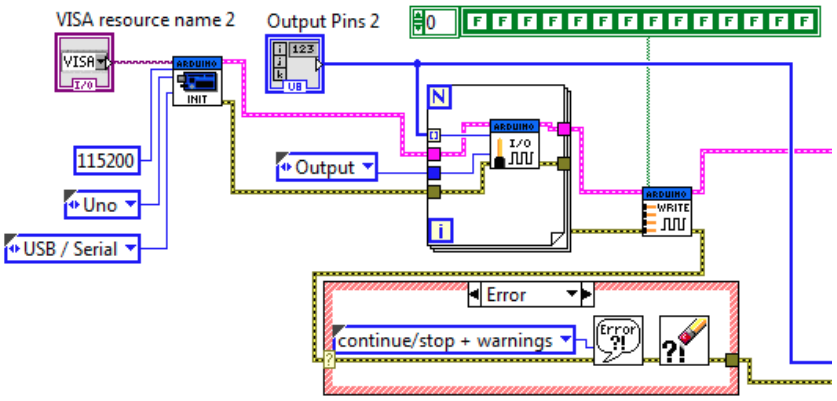


Figure 4.2: LabVIEW program responsible for initializing Arduino.

Figure 4.3 shows the respective LabView event case for one of the relays, where the relay is activated according to the value of its corresponding user interface button. It also queries the arduino to verify if the pin has been set as requested. For the others relays, the event case is similar.

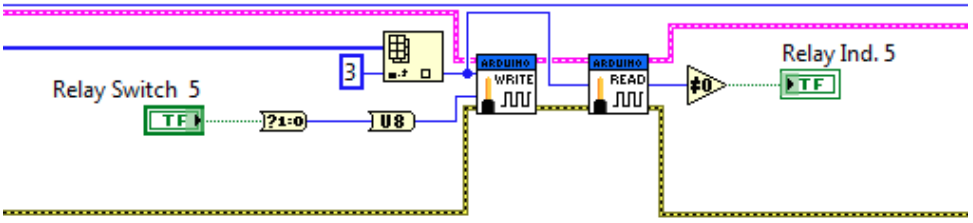


Figure 4.3: LabVIEW event case corresponding to one relay.

4.2.2 Resistor Control and Oscilloscope Data Acquisiton

In order to acquire data repeatably and in the most automated possible way, the LabView Interface for Arduino UNO was implemented in the previous program, adapted to acquire oscilloscope data (LabView Interface for Texmaker Oscilloscope). This enables to simultaneously acquire data from the oscilloscope and control the relays, using the same user interface. Thus,

it facilitates the data acquisition process for the study of the output power of the tribo-pairs and the planned subsequent device.

The result of the user interface is shown in Fig. 4.4 and in Appendix B different parts of the program are represented. The program is divided in three standard sections: inicialization, main cycle and closing, following an event based state machine architecture. It starts by initializing the oscilloscope and Arduino (Fig. B.1), assuring that no errors occur and that every pin is set to zero. The main cycle was made using an event structure. Thus, an event is created whenever a button is pressed on the front panel, which is handled through the event structure (Fig. B.3). These event cases grant the possibility of selecting the 12 relays, verify which Arduino pins are open (by pressing *update* on the frontpanel), and acquire oscilloscope data (as explained previously). There are two more event cases, one that remains timed out while instructions are not recieved and another that stops the program (by pressing *Stop* on the front panel).

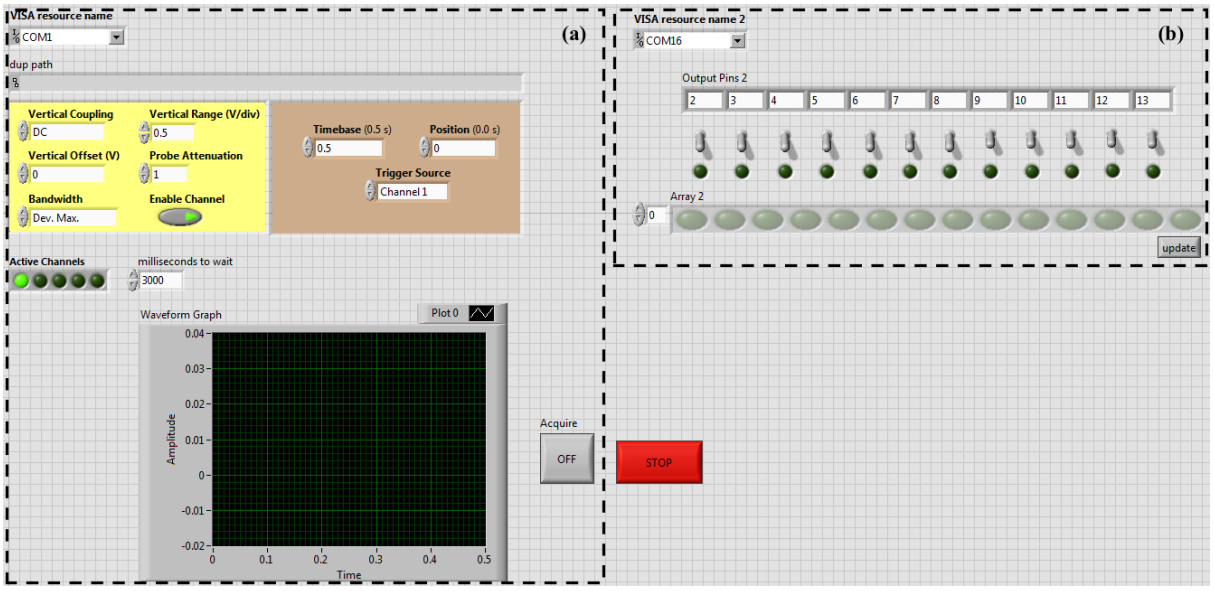


Figure 4.4: LabVIEW frontpanel for (a) oscilloscope data acquisition and (b) control of the relays.

This way, a scan of all the resistors was made, by selecting each relay individually. The channel 1 of the oscilloscope was used to acquire the open-circuit output voltage, while channel 2 was used to acquire the short-circuit output voltage, allowing to calculate the short-circuit output current, afterwards, and consequently its output power.

Chapter 5

Triboelectric-based device: harvesting energy from the environment

This chapter culminates all the studies performed in the previous ones in a prototype of a triboelectric device that harvests energy from the contact between two triboelectric materials, as a result of the magnetic force between a ferromagnetic ball and a magnetic tape. All the steps behind the construction of the device and results from the performed tests are detailed, by using data acquisition and resistor control programs for the analysis of the output power of the device.

Ordinarily, the triboelectric nanogenerators needs a rather dry environment in order to provide a stable output, since the surface triboelectrification would be reduce due to the presence of water [58]. Nevertheless, it is not out of the question, but even on the contrary, to incorporate this technology in water-related energy sources, like ocean waves, waterfalls, rainwater. This would be actually quite profitable since these are all abundant and inexhaustible sources of energy, and a good canditate as an alternative to solar energy harvesting. With this in mind, it is our aim to explore a new TENG prototype that can reliably convert water-source-related energy into electricity.

5.1 Experimental Details

For the construction of this device it was necessary to accurately plan its design and know the available materials, both for its construction and for deciding the one with the best triboelectric properties to harvest energy from. It should also be noted that the experimental prototype was projected and assembled from the start.

5.1.1 Device Design and Development

The basic principle behind the development of the device consists in harnessing the triboelectric effect of tribo-pairs via the magnetic coupling between a ferromagnetic ball and up to eight magnetic tapes. The device configuration essentially consists in a ferromagnetic ball within a cylindrical box and eight beams containing triboelectric materials attached to magnetic tapes.

In more detail, Fig. 5.1(a) shows a sketch of the initially projected device. Each beam has, at is end, a triboelectric material. A magnetic tape is then glued to the back part of each

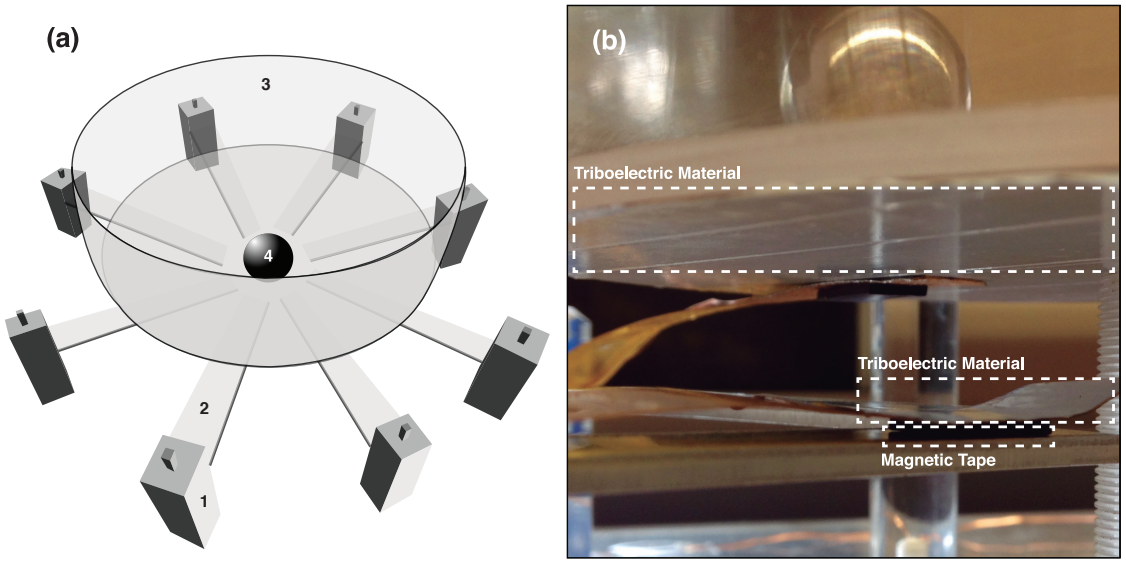


Figure 5.1: Triboelectric device: (a) Schematic diagram: **1** Suport (height 7 cm), **2** Beam (length 15 cm), **3** Cylindrical Box (height 7 cm; diameter 10 cm), **4** Ferromagnetic Ball (diameter 2.5 cm); (b) Details of the triboelectric materials and the magnetic tape.

triboelectric material and attached to the free end of the beam. Another triboelectic material is placed at the back of the base of the cylindrical box so that, when the ball passes on top of the

magnetic tape and attracts it, these two triboelectric materials get in contact producing energy [Fig. 5.1(b)].

With the purpose of maximizing the usable area of the cylinder base, eight beams were arranged. However, for testing purposes, only four beams were used, since it made the adjustment and alignment easier. The materials atop the four beams, are connected to the aluminium electrodes, which in turn are connected to electrical contacts. It was thus possible to link the four beams in series to maximize the obtained output voltage values. However, if the purpose was to obtain higher currents, these materials would had to be placed in parallel. The beams could be adjusted to five possible heights [with intervals of 0.6 cm; Fig. 5.2(a)].

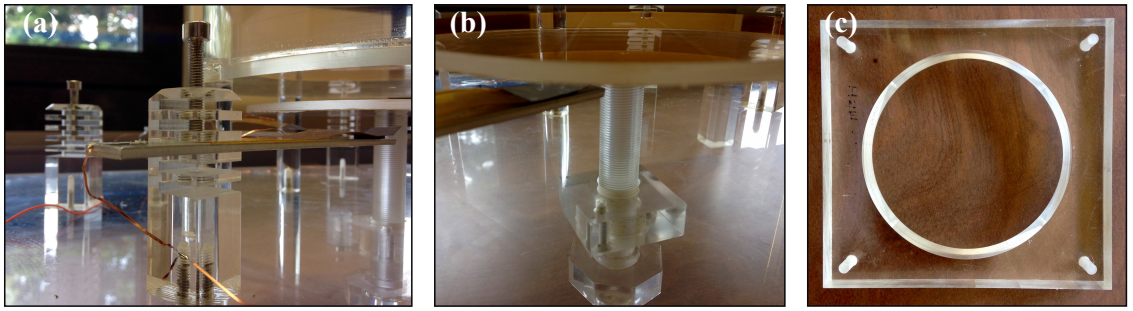


Figure 5.2: Elements of the prototype device: (a) beam support, (b) movable base and (c) section that reduces the area of the plate where the ball moves.

Afterwards, it was necessary to install a movable base beneath the ball's cage [Fig. 5.2(b)] to replace the cylinder fixed base where the triboelectric material is placed. This was changed because the force between the ball and the magnetic tape was too large in the case of the cylinder fixed base, so that only abrupt movements made the two magnetic elements detach. By introducing this movable base, it was possible to determine the ideal distance that minimizes this force, although maintaining the same output.

The movement of the ball on the plate will only result in a triboelectric output when the ball passes on the top of the magnetic tape. Since only four beams were used, most of the time the ball moved in an area where the magnetic tape was absent. Thus, another modification to the initial prototype was performed, aiming to limit the movement of the ball by reducing the area of the plate where the ball moved. This was done by adding a section represented in Fig. 5.2(c), the area then decreased from $\sim 314.2\ cm^2$ to $\sim 78.5\ cm^2$. This configuration is identical to a smaller cylinder with only four beams that support the triboelectric materials.

The final configuration of the prototype and respective details in which the tests were done is represented in Fig. 5.3.

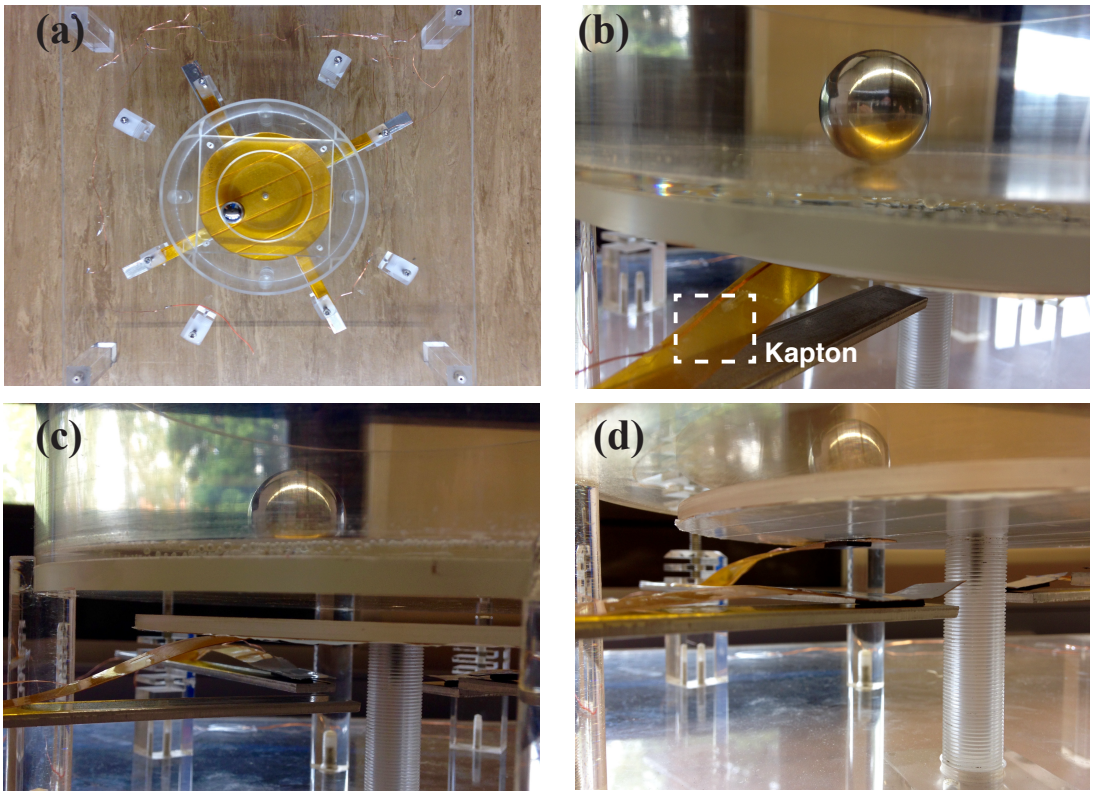


Figure 5.3: Final configuration of the prototype and some respective details.

5.1.2 Materials

5.1.2.1 Construction materials

Almost every device component (base, cylinder, movable base, supports, etc.) were built in acrylic since it is versatile and completely transparent (up to 92% light transmission), which eases the alignment of the beams to the effective area of the rotative base (where the ball spends most of the time), and it also provides a clear view of all the components of the device during the tests. Its other advantages include: it is nonmagnetic, has a high durability, excelent moldability during thermoforming, and has a large break resistance without the tendency to fragmentate. It has a low relative density of $1.19\ g/cm^3$, compared with other considered construction materials [59]: an acrylic beam has about half the weight of an equivalent glass beam. It retains around 2% of the humidity and only 0.35%, at most, contributes to a volume increase, which is an excellent property in the cases it is applied in contact with water.

In relation to the beams that secure the triboelectric materials, aluminium, which is also nonmagnetic, was chosen. Since it is less flexible than acrylic, and therefore not as susceptible to deformation (which can happen due to the force applied by the material on the support after

ball decoupling). Kapton, being very flexible, was used as link between the beam and the set constituted by the triboelectric material, electrode and magnetic tape, as represented in Fig. 5.3(b). It should also be noted that every screw is non magnetic, and the ferromagnetic ball is made of steel.

5.1.2.2 Triboelectric materials

Choosing two materials that are largely separated in the triboelectric series will result in a higher performance device. This way, according to the available materials it was determined, with the aid of the triboelectric table and the testing system (Chapter 3), that the tribo-pair Nylon/PTFE in sheet form are the most appropriate for the device, due to their flexibility, resistance, and readiness to use. Every beam contained the same material, PTFE, with the same dimensions (1.5×3 cm^2) and the movable base was completely filled with Nylon.

It is possible to substitute one, or even two, materials of the tribo-pair for texturized ones, such as PDMS, in order to enhance the output power of the device. However, this was not performed during this project.

5.1.3 Set-up and Measurements

To test the developed device's performance it was necessary to assemble an experimental set-up that, along with the program developed in LabView (described in subsection 4.2.2), allowed acquiring data for a detailed analysis of the characteristics of the device. More specifically, the purpose of performing the tests is to obtain the output power of the device. Therefore, these tests were divided in three steps: i) measurement of the open-circuit output voltage (V_{OC}); ii) measurement of the short-circuit output voltage (V_{SC}); iii) calculation of the output power.

Figure 5.4(a) shows the experimental set-up used for testing the device. The test were conducted on a testing table, with a circular a motion in the xy plane [Fig. 5.4(b)]. The testing table makes the magnetic ball move, attracting, one at a time, the four triboelectric materials. The device's electric contacts are linked to a circuit board, with a wide range of resistors, controlled by relays. These are handled by an Arduino UNO (connected to the available digital pins) and fed through a 6 V voltage source.

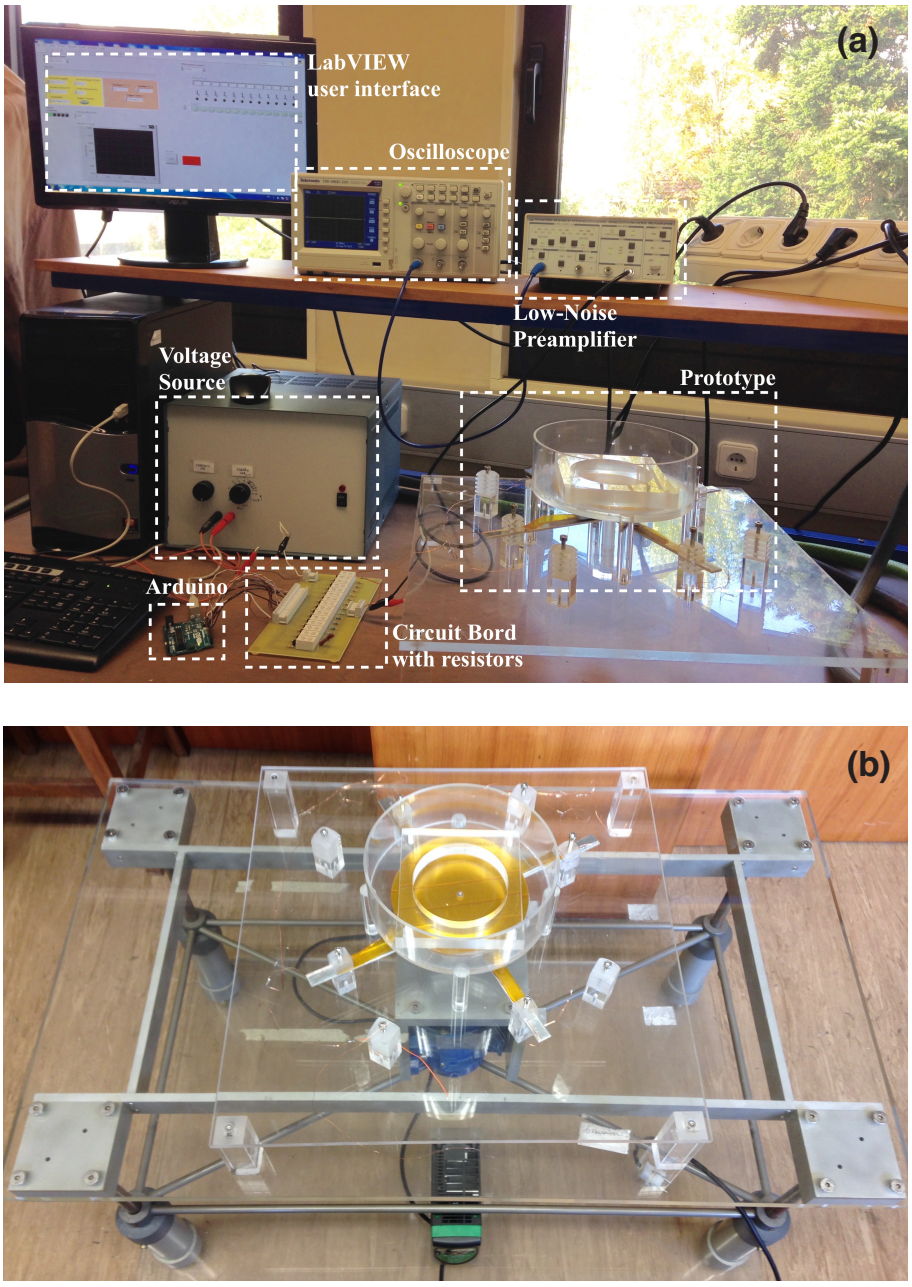


Figure 5.4: (a) Experimental set-up of the triboelectric device and (b) the testing table.

The first measurement was taken under open-circuit conditions, and the oscilloscope is connected to the electric contacts in channel 1. Both the oscilloscope and the Arduino UNO connect to the computer through an USB port and are controlled by the LabView program, detailed in subsection 4.2.2.

With the second measurement, and applying Ohm's Law, the short-circuit output current (I_{SC}) was calculated. A SR560 Low-Noise Preamplifier [60], connected to the oscilloscope, in channel 2, was used to amplify the small voltage peaks. Therefore, the low-noise preamplifier

was configured (on its front panel) with a high-pass and low-pass filter at $+6\ dB/octave$ each, and cutoff frequencies of $10\ Hz$ and $3\ kHz$, respectively. After performing experimental tests to determine the value for the minimum necessary gain and taking into account the gain settings available, the instrument's gain was set to 200. This way, in order to measure the short-circuit output voltage, the oscilloscope measures the voltage drop on a resistor of $(10.1 \pm 0.1)\ \Omega$ placed on the circuit board. The short-circuit current was then calculated using $I_{SC} = \frac{V_{SC}}{10.1}$.

To obtain the output power of the device (third step), every resistor of the circuit board (section 4.2) was scanned measuring, one at a time, both output voltage and current, acquiring various oscilloscope "windows" for each resistor. The output power was then calculated simply using

$$P = VI \tag{5.1}$$

All the measurements were repeated for four different distances (d) between the ferromagnetic ball and the magnetic tape: $d_1 = 2.2$, $d_2 = 2.8$, $d_3 = 3.4$ and $d_4 = 4\ cm$. The distance d_1 corresponds to the minimum possible value for this configuration, and the distance d_4 corresponds to the maximum, since a larger distance leads to no coupling between the ferromagnetic ball and the magnetic tape.

5.2 Experimental Results

5.2.1 Open-Circuit Voltage and Short-Circuit Current

As mentioned, the measurements were performed for four distances between the ball and the magnetic tape. Foremost, the values of the open-circuit voltage peaks were registered for each distance d. One example of the acquired windows for each distance is presented in Fig. 5.5.

Each peak corresponds to the contact between tribo-pairs, with one cycle having four main peaks, since there are four beams and therefore four tribo-pairs. As the voltage peaks of each acquisition were not constant, their average was taken instead. It is verified that, for the smaller distance d_1, the voltage peaks has the lowest values, with the smallest peak having $\sim 1\ V$. The highest voltage peak is detected for the distance d_2, $\sim 8.6\ V$. However, the distance d_3 provides the most uniforme peak values. Since approximately 10 oscilloscope windows were attained for each distance, an average of the peak values was calculated for all registered

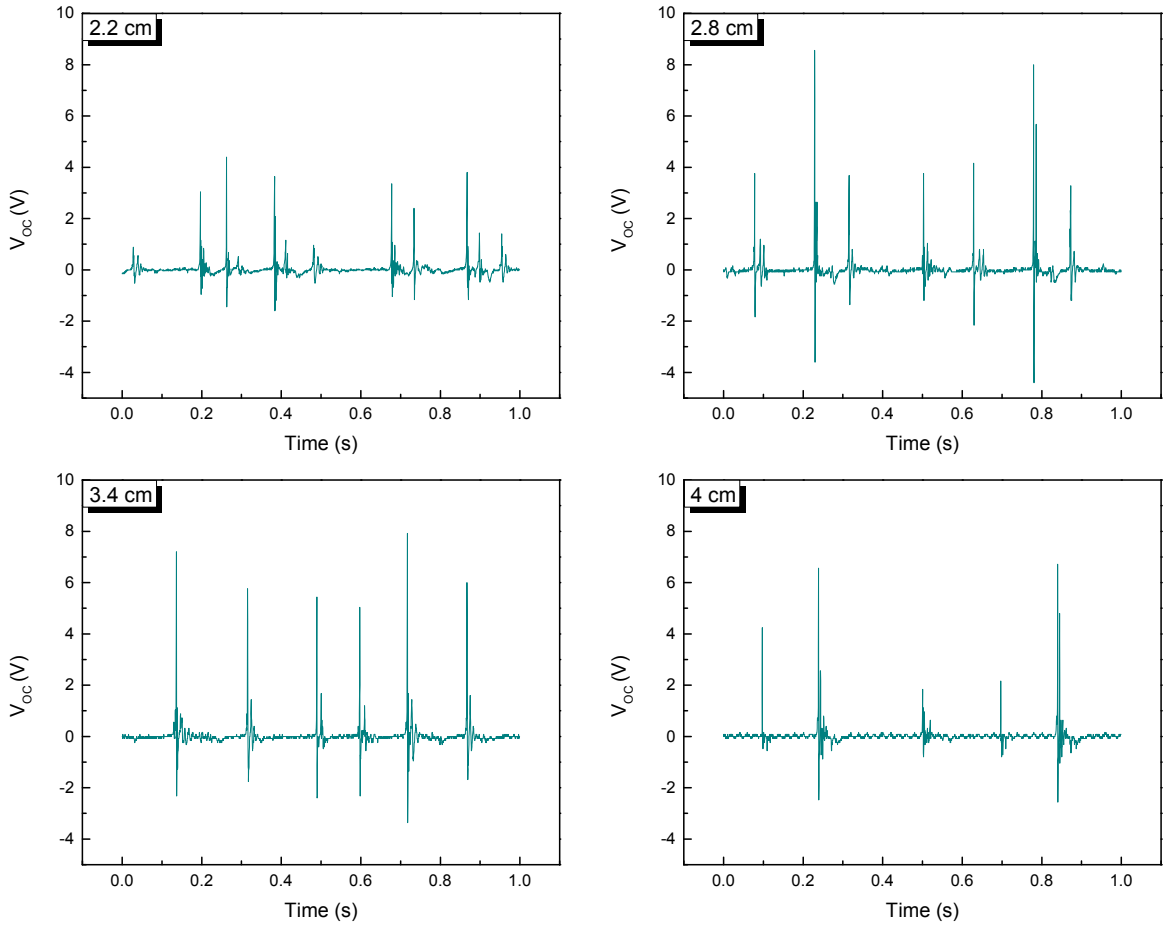


Figure 5.5: Open-circuit voltage peaks for four distances between the ferromagnetic ball and the magnetic tape.

windows, resulting in the graph represented in Fig. 5.6(a). The highest average output voltage, $< V_{OC} >$, was obtained for d_2 and d_3, with the highest average corresponding to the distance $d_3 = 3.4\ cm, \sim 4.2\ V$.

In Fig. 5.6(b) we can observe the shape of a representative voltage peak for d_3. There are clearly two peaks that result from the contact mode. The first (1 and 2) is related to the contact for the region of the tribo-pair materials with the highest surface area. The other one can result from smaller regions of the surface of the materials that only become in contact after the larger region.

In Fig. 5.7 is represented an example of one of the acquired oscilloscope windows for each of the distances relatively to the short-circuit current peaks. Once more, the distance d_3 has shown to be more stable despite that the highest current peak being observed in d_2.

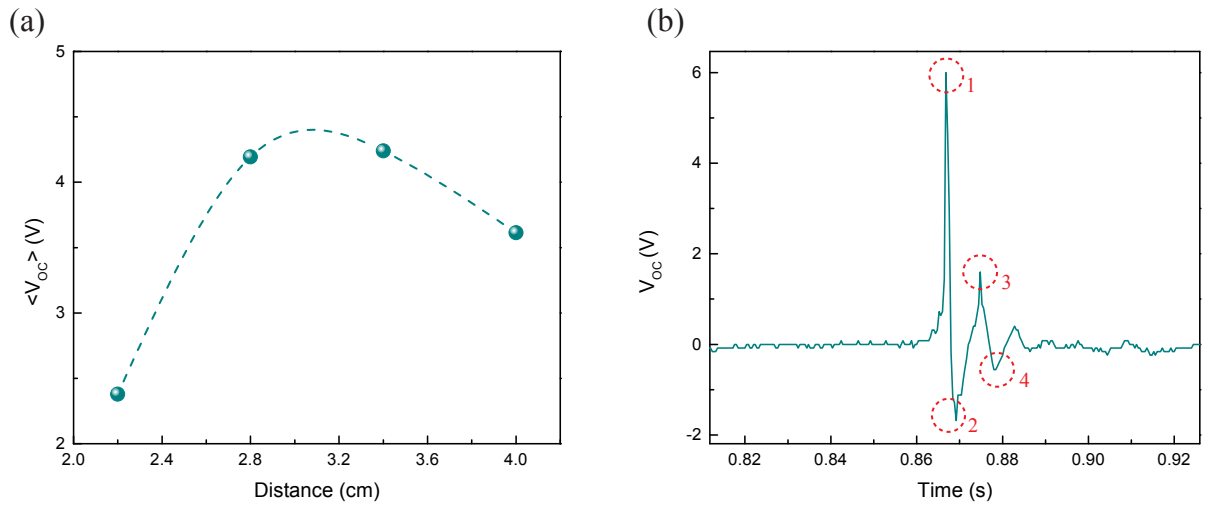


Figure 5.6: (a) The dependence of open-circuit voltage with the four distances between the ferromagnetic ball and the magnetic tape. (b) Magnification of a peak voltage from the d_3 distance.

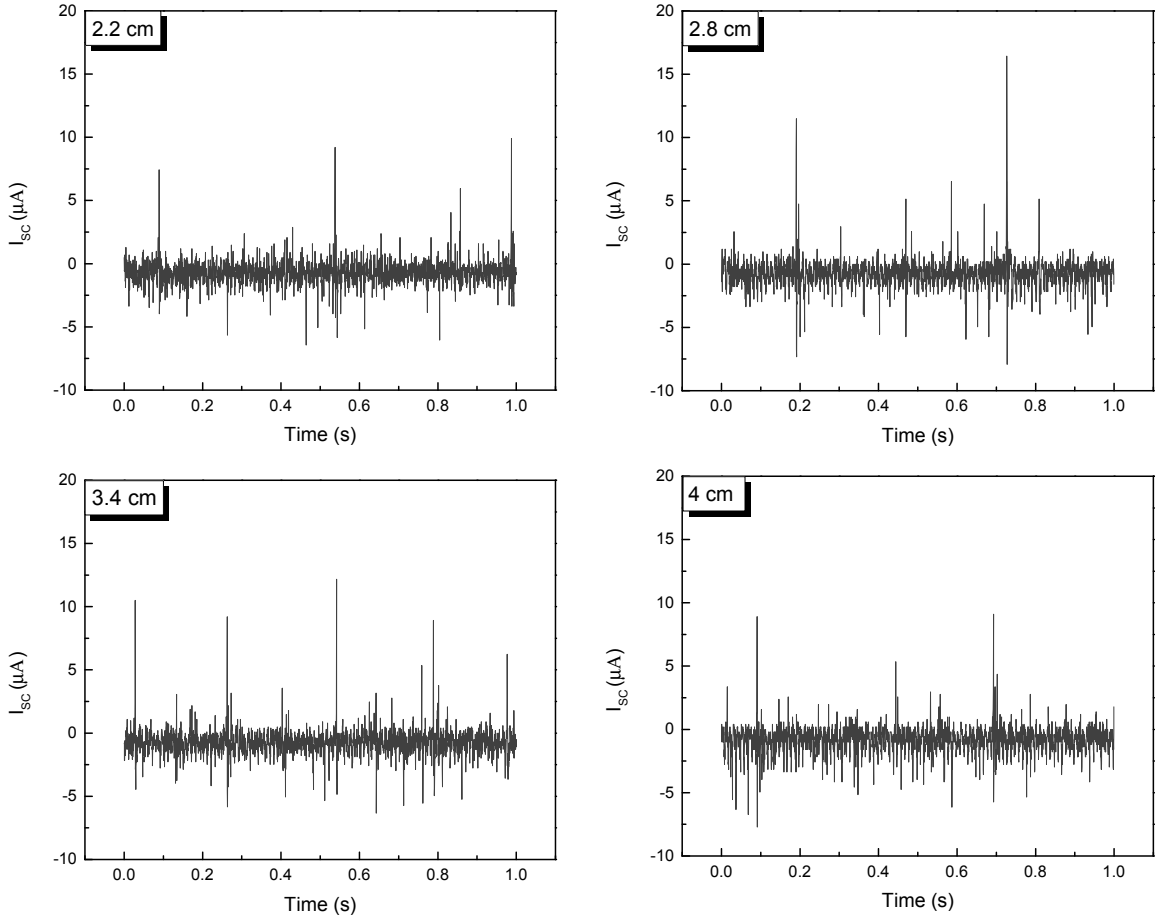


Figure 5.7: Short-circuit current peaks for four distances between the ferromagnetic ball and the magnetic tape.

Distance (cm)	$< I_{SC} >$ (μA)
2.2	6.14
2.8	7.18
3.4	6.30
4	6.27

Table 5.1: Mean short-circuit output currents for four distances between the ferromagnetic ball and the magnetic tape.

The weight of the distance in the average of the short-circuit output current is made clear in the table 5.1. It is verified that the fluctuation of the values of the current is minimal, although it is slightly higher for the distance d_2, $< I_{SC} > \sim 7.18\ \mu A$, followed by d_3, with $< I_{SC} > \sim 6.30\ \mu A$.

5.2.2 Output Power

To fully characterize the system, the electric outputs were measured using a wide array of variable load resistors, with values between $100\ \Omega$ and $5\ G\Omega$. Various 1 second windows were registered from the oscilloscope for every single resistor of the circuit board. Figure 5.8 shows the resistance dependence of both output current and voltage, from $100\ \Omega$ to $5\ G\Omega$. The output currents decrease with increasing load resistance, while the output voltages show the reverse trend. Performing a more detailed analysis, it is clear that these charts follow a *three-working-region* behaviour [30]. In Region I (Fig. 5.8; graph 3.4 cm), where the resistance is low ($0.1 - 100$ kΩ), the output characteristics are close to the short-circuit condition [$V = 0$ from Eq. (2.1)]. On the other hand, when the resistor is larger than $1\ G\Omega$ (Region III), the output characteristics are close to the open-circuit condition, in which the maximum voltage saturates at V_{OC}. For Region II, the maximum current drops dramatically, but the maximum voltage increases at a reverse trend. Around 1 MΩ the device reaches its maximum instantaneous output power.

This *three-working-region* behaviour can be physically interpreted. After the contact, the two triboelectric materials separate immediately, generating an induced voltage between the two electrodes, which drive the electrons from one electrode to the other. Therefore, the charge accumulation rate at short-circuit condition is the maximum charge transfer rate ($Q \sim Q_{SC}$ in Region I). However, as there is an external load resistance, the resistor will limit the real charge transfer rate, making it lower than that at short-circuit condition. When the load resistor is large enough (Region III) the electron transfer is rather slow, which results in a very small current. In

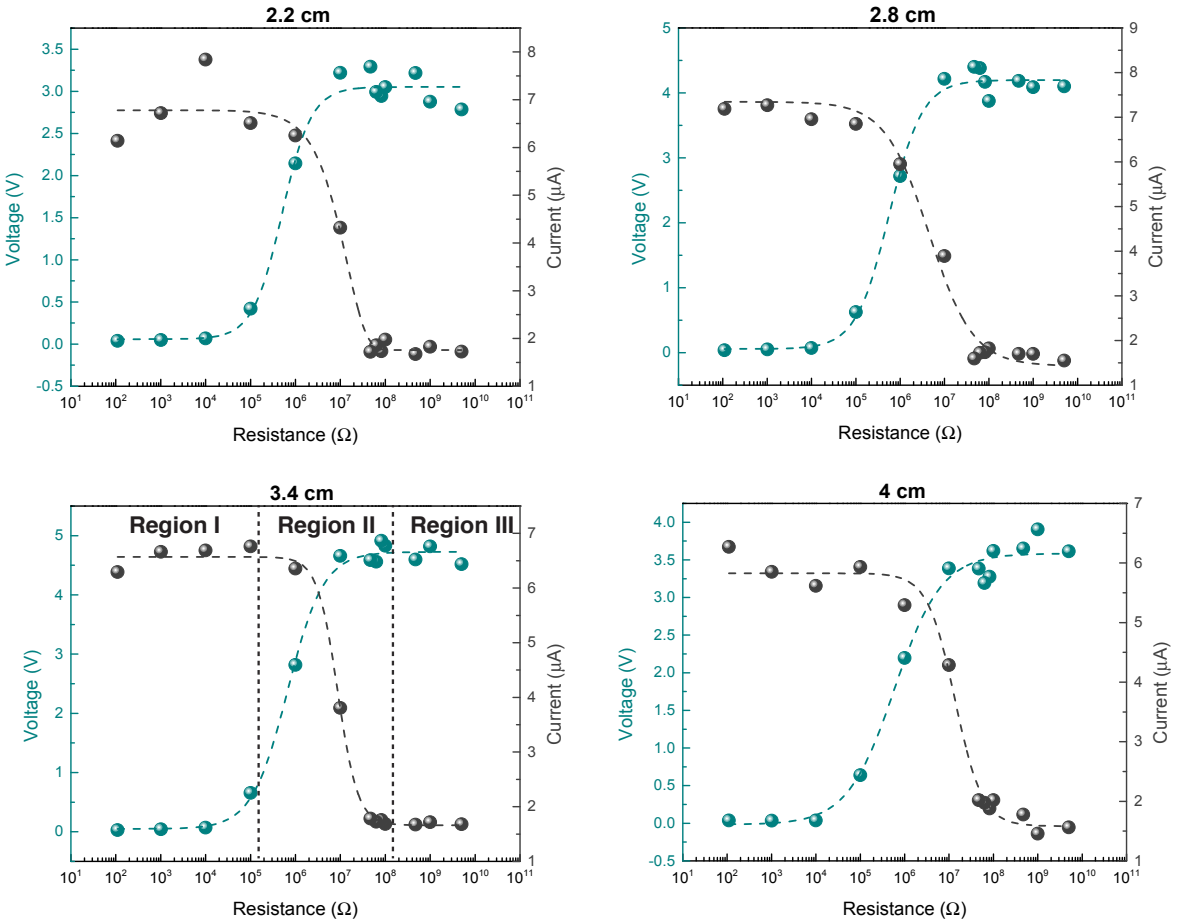


Figure 5.8: The dependence the output voltage and current on the external loading resistors.

the opposite side, the induced voltage between the two electrodes approach to V_{OC} due to the little screening effect.

Besides this explanation, this behaviour can also be understood through the impedance of the system (inherent TENG capacitance and load resistance). In the case that the load resistance is small, its impedance is much lower than the impedance of the TENG capacitance. Hence, the total impedance is ruled by the TENG inherent capacitance and the output current is practically unchanged when the resistance rises. When the load resistance is large enough, its impedance turns much larger than that of the TENG capacitance. This way, almost all of the V_{OC} is applied on the load resistance and the TENG works under a near open-circuit condition. The maximum transit power is attained when the load resistance is in the middle region, that is, when it matches the TENG impedance.

Actually, it was expected that the value of the current would be essentially zero for high resistances (Fig. 5.8; Region III). However, that is not what was observed as the value obtained

for those resistances is approximately the same as that of the circuit noise in open-circuit.

The power outputs are also plotted as a function of the external resistance in Fig. 5.9. The output power reached a maximum value of nearly $17.7\ \mu W$ (or $0.04\ W/m^2$) at a load of 1 MΩ (as expected by the previous analysis). This shows that the favored distance for this device is

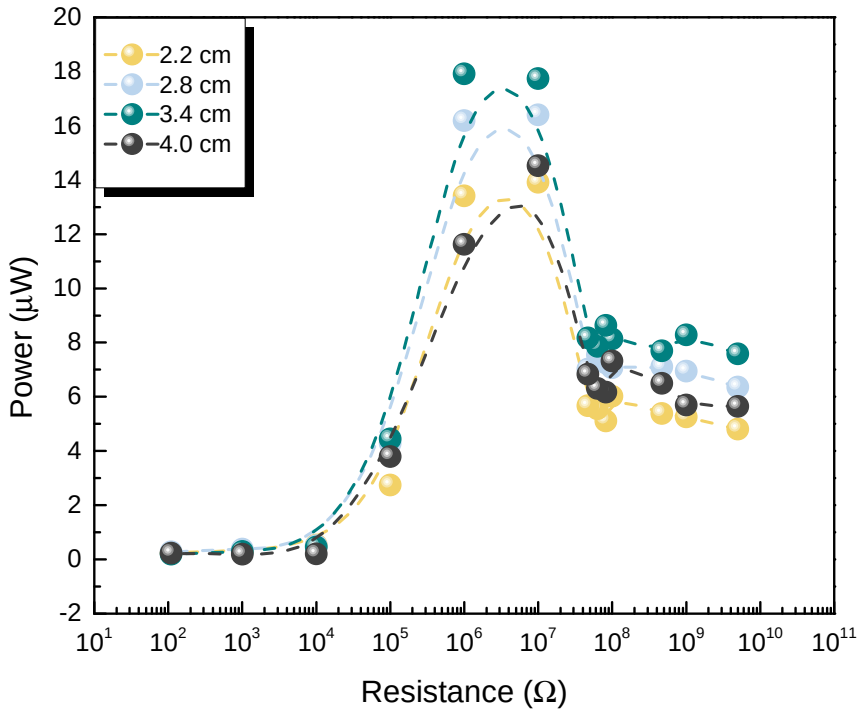


Figure 5.9: The dependence of the output power on the external loading resistors.

d_3, since it exhibited larger impact force than d_1 and d_2, larger area of contact than d_4, and an overall more stable current.

5.3 Summary

We built a prototype whose configuration allows to harvest energy from the contact between triboelectric materials, as a result of magnetic coupling between a ferromagnetic ball and a magnetic tape. Both the device development and the experimental set-up was projected and assembled from the start.

Tests were made to characterize the device for the four beams configuration and also for four different distances between the ferromagnetic ball and the magnetic tape. The data was

acquired through a Labview program. Analyzing the dependence of the open-circuit voltage and short-circuit current on the distance between the ferromagnetic ball and the magnetic tape, it was possible to conclude that our device has the best performance, for $d_3 = 3.4$ cm. For this distance we obtained $< V_{OC} > \simeq 4.2\ V$ and $< I_{SC} > \sim 6.3\ \mu A$, however, the output current mean for d_2 was slightly higher.

The electric outputs were also measured using a wide array of variable load resistors ($100\ \Omega$ - $5\ G\Omega$). These measurements revealed a *three-working-region* behavior, which can be explained both from the charge transfer rate and system impedance point of views. The output power value at each resistance was calculated using P = IV. The maximum value of $17.7\ \mu W$ (or $0.04\ W/m^2$) at a load resistance of 1 MΩ was obtained for the d_3 distance, demonstrating that the device's performance is better for this distance.

This device is ultimately a successful proof of concept prototype. However, it still needs to be further improved, including the enhancement of the effective contact area of the tribo-pairs, and testing with other configurations, such as using eight beams.

Chapter 6

Conclusions and Future Directions

6.1 Conclusions

Energy harvesting devices are the new highlight in nanotechnology, setting aside traditional power supplies such as batteries. Triboelectric nanogenerators are based on contact electrification effect and electrostatic induction, i.e. the triboelectric effect, which is a universally known, but still somewhat mysterious, phenomenon. The contact between two materials with different triboelectric polarities result in the transference of electron/ion/materials between the materials surface, creating an electric potential difference after their separation. By cyclically contacting and separating materials with oppositely charged surfaces, electrons are driven to flow through the external load, generating a continous output. There, the main objective was to incorporate this technology in water-related energy sources, particullarly, taking advantage of the mechanical energy inherent to the motion of water.

Before beginning constructing the device, it was necessary to make a comprehensive study of the materials, which involved building a testing system. Additionally, in order to increase the triboelectrification effect we performed the successful texturizing of the surface of the PDMS, using two different methods: Nanoporous Aluminium Templates and Micromachined Silicon Molds. The testing system allowed the verification that the best triboelectric pair is Nylon and PTFE, the materials, from the ones that were available, that were placed farther away from each other in the triboelectric series. Relatively to the texturized materials, we obtained an evident voltage increase of around 100.0% for both the textured samples. From this, it is possible to claim that the texturization increases the effectiveness of the friction area, and, consequently, of the triboelectric effect.

The built prototype allows harvesting energy from the contact between triboelectric materials, as a result of magnetic coupling between a ferromagnetic ball and a magnetic tape. Its operation mode results from the hybridization of contact-sliding-separation-contact processes. Tests were made to characterize the device for the four beam configuration and also for four different distances between the ferromagnetic ball and the magnetic tape. It was concluded that our device has the best performance, for $d_3 = 3.4$ cm with $< V_{OC} > \simeq 4.2\ V$, $< I_{SC} > \sim 6.3\ \mu A$, and a maximum value of $17.7\ \mu W$ (or $0.04\ W/m^2$) at a load resistance of 10 MΩ.

This project allowed developing a triboelectric device, which later revealed to be, ultimately, a successful proof of concept prototype. As such, the relevance of this work, in its current state, is recognized as a basis for the development of other, more efficient, devices with different applications related to exploiting the energy carried by ocean surface waves.

6.2 Future Directions

In future development one expects more testing around the optimal configuration of the device, namely, shifting the number of beams, and finding a way to turn the contact area of each tribo-pair more efficient. It is also necessary to adjust the tribo-pairs so that their individual output are as identical as possible, since in the performed tests it was noticed that two of them had remarkably worse results. Preparing another type of tests is also one aim, for example, instead of making the table spin on the *xy* plane, make it rotate on three dimensions, and, most importantly, test the device in an environment closer to its intended application, as a wave energy converter. Furthermore, improving the fabrication of triboelectric nanogenerators for a more efficient energy storage, by improving the efficiency of nano- and micro- structured triboelectric materials is also a major aim. Moreover, it is still required to uncover a concrete way to best use the energy produced through this system, for example, using it to power, indefinitely, ”warning signs” in the middle of the ocean.

Bibliography

[1] Z. Wang, *Nanogenerators for self-powered devices and systems*. 2011. (Cited on page ↑1.)

[2] P. L. Menezes, C. J. Reeves, and M. R. Lovell, *Tribology for Scientists and Engineers*. 2013. (Cited on page ↑5.)

[3] P. F. O'grady, "Thales of miletus the beginnings of western science and philosophy," 2002. (Cited on page ↑5.)

[4] "A Natural History: Devin Corbin." (Cited on page ↑5.)

[5] J. C. Wilcke, *Disputatio Physica Experimentalis, De Electricitatibus Contrariis*. 1757. (Cited on page ↑5.)

[6] Z. L. Wang, "Triboelectric Nanogenerators as New Energy Technology for Self-Powered Chemical Sensors," no. 11, pp. 9533–9557, 2013. (Cited on pages ↑6, ↑10, ↑19, and ↑22.)

[7] "Triboelectric Series."

[8] D. M. Gooding and G. K. Kaufman, "Tribocharging and the triboelectric series," *Encyclopedia of Inorganic and Bioinorganic Chemistry*, 2014. (Cited on page ↑6.)

[9] B. Bhushan, *Introduction to Tribology, Second Edition*. 2013. (Cited on pages ↑6 and ↑9.)

[10] J. Lowell and A. C. Rose-Innes, "Contact electrification," *Advances in Physics*, pp. 37–41, 1980. (Cited on pages ↑7 and ↑11.)

[11] D. J. Lacks and R. M. Sankaran, "Contact electrification of insulating materials," *Journal of Physics D: Applied Physics*, vol. 44, no. 45, p. 453001, 2011. (Cited on page ↑7.)

[12] M. W. Williams, "Triboelectric charging of insulating polymers–some new perspectives," *AIP Advances*, vol. 2, no. 1, p. 010701, 2012. (Cited on page ↑7.)

[13] H. Mizes, E. Conwell, and D. Salamida, "Direct observation of ion transfer in contact charging between a metal and a polymer," *Applied physics letters*, vol. 56, no. 16, pp. 1597–1599, 1990. (Cited on page ↑8.)

[14] Y. Yang, W. Guo, K. C. Pradel, G. Zhu, Y. Zhou, Y. Zhang, Y. Hu, L. Lin, and Z. L. Wang, "Pyroelectric nanogenerators for harvesting thermoelectric energy," *Nano Letters*, vol. 12, no. 6, pp. 2833–2838, 2012. (Cited on page ↑9.)

[15] M.-Y. Choi, D. Choi, M.-J. Jin, I. Kim, S.-H. Kim, J.-Y. Choi, S. Y. Lee, J. M. Kim, and S.-W. Kim, "Mechanically powered transparent flexible charge-generating nanodevices with piezoelectric zno nanorods," *Advanced Materials*, vol. 21, no. 21, pp. 2185–2189, 2009. (Cited on pages ↑9 and ↑10.)

[16] L. J. Brillson and Y. Lu, "ZnO Schottky barriers and Ohmic contacts," *Journal of Applied Physics*, vol. 109, no. 12, 2011. (Cited on page ↑10.)

[17] S. Xu, Y. Qin, C. Xu, Y. Wei, R. Yang, and Z. L. Wang, "Self-powered nanowire devices.," *Nature nanotechnology*, vol. 5, no. 5, pp. 366–373, 2010. (Cited on page ↑10.)

[18] Z. L. Wang, "Towards self-powered nanosystems: From nanogenerators to nanopiezotronics," *Advanced Functional Materials*, vol. 18, no. 22, pp. 3553–3567, 2008. (Cited on page ↑10.)

[19] X. Wang and J. Shi, "Piezoelectric nanogenerators for self-powered nanodevices," in *Piezoelectric Nanomaterials for Biomedical Applications*, pp. 135–172, Springer, 2012. (Cited on page ↑10.)

[20] G. Cheng, Z.-H. Lin, Z.-l. Du, and Z. L. Wang, "Simultaneously harvesting electrostatic and mechanical energies from flowing water by a hybridized triboelectric nanogenerator," *ACS nano*, vol. 8, no. 2, pp. 1932–1939, 2014. (Cited on page ↑11.)

[21] G. Zhu, C. Pan, W. Guo, C. Y. Chen, Y. Zhou, R. Yu, and Z. L. Wang, "Triboelectric-generator-driven pulse electrodeposition for micropatterning," *Nano Letters*, vol. 12, no. 9, pp. 4960–4965, 2012. (Cited on pages ↑11, ↑14, and ↑15.)

[22] G. Zhu, Z. H. Lin, Q. Jing, P. Bai, C. Pan, Y. Yang, Y. Zhou, and Z. L. Wang, "Toward large-scale energy harvesting by a nanoparticle-enhanced triboelectric nanogenerator," *Nano Letters*, vol. 13, no. 2, pp. 847–853, 2013. (Cited on pages ↑11 and ↑12.)

[23] Y. Yang, L. Lin, Y. Zhang, Q. Jing, T. C. Hou, and Z. L. Wang, "Self-powered magnetic sensor based on a triboelectric nanogenerator," *ACS Nano*, vol. 6, no. 11, pp. 10378–10383, 2012. (Cited on page ↑11.)

[24] Z. L. Wang, "Triboelectric nanogenerators as new energy technology for self-powered systems and as active mechanical and chemical sensors," *ACS Nano*, vol. 7, no. 11, pp. 9533–9557, 2013. (Cited on page ↑11.)

[25] Z. H. Lin, G. Cheng, L. Lin, S. Lee, and Z. L. Wang, "Water-solid surface contact electrification and its use for harvesting liquid-wave energy," *Angewandte Chemie - International Edition*, vol. 52, no. 48, pp. 12545–12549, 2013. (Cited on page ↑11.)

[26] F. R. Fan, L. Lin, G. Zhu, W. Wu, R. Zhang, and Z. L. Wang, "Transparent triboelectric nanogenerators and self-powered pressure sensors based on micropatterned plastic films," *Nano Letters*, vol. 12, no. 6, pp. 3109–3114, 2012. (Cited on pages ↑12, ↑22, and ↑33.)

[27] S. Niu, Y. Liu, S. Wang, L. Lin, Y. S. Zhou, Y. Hu, and Z. L. Wang, "Theory of sliding-mode triboelectric nanogenerators," *Advanced Materials*, vol. 25, no. 43, pp. 6184–6193, 2013. (Cited on pages ↑12 and ↑16.)

[28] "Harvesting Electricity: Triboelectric Generators Capture Wasted Power." (Cited on pages ↑12 and ↑17.)

[29] S. Niu, Y. Liu, S. Wang, L. Lin, Y. S. Zhou, Y. Hu, and Z. L. Wang, "Theoretical investigation and structural optimization of single-electrode triboelectric nanogenerators," *Advanced Functional Materials*, vol. 24, no. 22, pp. 3332–3340, 2014. (Cited on pages ↑13 and ↑14.)

[30] S. Niu and Z. L. Wang, "Theoretical systems of triboelectric nanogenerators," *Nano Energy*, 2014. (Cited on pages ↑21 and ↑54.)

[31] S. Niu, S. Wang, L. Lin, Y. Liu, Y. S. Zhou, Y. Hu, and Z. L. Wang, "Theoretical study of contact-mode triboelectric nanogenerators as an effective power source," *Energy & Environmental Science*, vol. 6, no. 12, pp. 3576–3583, 2013. (Cited on page ↑14.)

[32] S. Wang, L. Lin, Y. Xie, Q. Jing, S. Niu, and Z. L. Wang, "Sliding-triboelectric nanogenerators based on in-plane charge-separation mechanism," *Nano Letters*, vol. 13, no. 5, pp. 2226–2233, 2013. (Cited on pages ↑16, ↑17, ↑18, and ↑19.)

[33] L. Lin, S. Wang, Y. Xie, Q. Jing, S. Niu, Y. Hu, and Z. L. Wang, "Segmentally structured disk triboelectric nanogenerator for harvesting rotational mechanical energy," *Nano Letters*, vol. 13, no. 6, pp. 2916–2923, 2013. (Cited on pages ↑16 and ↑18.)

[34] P. Bai, G. Zhu, Y. Liu, J. Chen, Q. Jing, W. Yang, J. Ma, G. Zhang, and Z. L. Wang, "Cylindrical rotating triboelectric nanogenerator," *ACS Nano*, vol. 7, no. 7, pp. 6361–6366, 2013. (Cited on pages ↑17 and ↑18.)

[35] Y. Yang, Y. S. Zhou, H. Zhang, Y. Liu, S. Lee, and Z. L. Wang, "A single-electrode based triboelectric nanogenerator as self-powered tracking system," *Advanced Materials*, vol. 25, no. 45, pp. 6594–6601, 2013. (Cited on page ↑19.)

[36] Y. Yang, H. Zhang, J. Chen, Q. Jing, Y. S. Zhou, X. Wen, and Z. L. Wang, "Single-electrode-based sliding triboelectric nanogenerator for self-powered displacement vector sensor system," *ACS Nano*, vol. 7, no. 8, pp. 7342–7351, 2013. (Cited on page ↑20.)

[37] H. Zhang, Y. Yang, X. Zhong, Y. Su, Y. Zhou, C. Hu, and Z. L. Wang, "Single-electrode-based rotating triboelectric nanogenerator for harvesting energy from tires," *ACS Nano*, vol. 8, no. 1, pp. 680–689, 2014. (Cited on page ↑20.)

[38] S. Wang, Y. Xie, S. Niu, L. Lin, and Z. L. Wang, "Freestanding triboelectric-layer-based nanogenerators for harvesting energy from a moving object or human motion in contact and non-contact modes," *Advanced Materials*, vol. 26, no. 18, pp. 2818–2824, 2014. (Cited on pages ↑20 and ↑21.)

[39] S. Wang, S. Niu, J. Yang, L. Lin, Z. L. Wang, and W. E. T. Al, "Quantitative Measurements of Vibration Amplitude Using a Contact-Mode Freestanding Triboelectric Nanogenerator," no. Xx, 2014. (Cited on page ↑21.)

[40] S. Wang, Y. Xie, S. Niu, L. Lin, C. Liu, Y. S. Zhou, and Z. L. Wang, "Maximum Surface Charge Density for Triboelectric Nanogenerators Achieved by Ionized-Air Injection: Methodology and Theoretical Understanding," *Advanced Materials*, pp. 6720–6728, 2014. (Cited on page ↑22.)

[41] W. Yang, J. Chen, G. Zhu, X. Wen, P. Bai, Y. Su, Y. Lin, and Z. Wang, "Harvesting vibration energy by a triple-cantilever based triboelectric nanogenerator," *Nano Research*, vol. 6, no. 12, pp. 880–886, 2013. (Cited on page ↑23.)

[42] J. Chen, G. Zhu, W. Yang, Q. Jing, P. Bai, Y. Yang, T. C. Hou, and Z. L. Wang, "Harmonic-resonator-based triboelectric nanogenerator as a sustainable power source and a self-powered active vibration sensor," *Advanced Materials*, vol. 25, no. 42, pp. 6094–6099, 2013. (Cited on page ↑23.)

[43] J. Yang, J. Chen, Y. Yang, H. Zhang, W. Yang, P. Bai, Y. Su, and Z. L. Wang, "Broadband vibrational energy harvesting based on a triboelectric nanogenerator," *Advanced Energy Materials*, vol. 4, no. 6, pp. 1–9, 2014. (Cited on page ↑23.)

[44] G. Zhu, P. Bai, J. Chen, and Z. Lin Wang, "Power-generating shoe insole based on triboelectric nanogenerators for self-powered consumer electronics," *Nano Energy*, vol. 2, no. 5, pp. 688–692, 2013. (Cited on pages ↑23 and ↑24.)

[45] W. Yang, J. Chen, G. Zhu, J. Yang, P. Bai, Y. Su, Q. Jing, X. Cao, and Z. L. Wang, "Harvesting energy from the natural vibration of human walking," *ACS Nano*, vol. 7, no. 12, pp. 11317–11324, 2013. (Cited on page ↑24.)

[46] Z. H. Lin, G. Zhu, Y. S. Zhou, Y. Yang, P. Bai, J. Chen, and Z. L. Wang, "A self-powered triboelectric nanosensor for mercury ion detection," *Angewandte Chemie - International Edition*, vol. 52, no. 19, pp. 5065–5069, 2013. (Cited on pages ↑24 and ↑25.)

[47] X. Cheng, B. Meng, X. Zhang, M. Han, Z. Su, and H. Zhang, "Wearable electrode-free triboelectric generator for harvesting biomechanical energy," *Nano Energy*, vol. 12, pp. 19–25, 2015. (Cited on page ↑24.)

[48] S. Lee, W. Ko, Y. Oh, J. Lee, G. Baek, Y. Lee, J. Sohn, S. Cha, J. Kim, J. Park, *et al.*, "Triboelectric energy harvester based on wearable textile platforms employing various surface morphologies," *Nano Energy*, vol. 12, pp. 410–418, 2015. (Cited on page ↑24.)

[49] Y. Zi, L. Lin, J. Wang, S. Wang, J. Chen, X. Fan, P.-K. Yang, F. Yi, and Z. L. Wang, "Triboelectric–pyroelectric–piezoelectric hybrid cell for high-efficiency energy-harvesting and self-powered sensing," *Advanced Materials*, vol. 27, no. 14, pp. 2340–2347, 2015. (Cited on page ↑25.)

[50] D. Bornside, C. Macosko, and L. Scriven, "Spin coating: One-dimensional model," *Journal of Applied Physics*, vol. 66, no. 11, pp. 5185–5193, 1989. (Cited on page ↑28.)

[51] Z. Zhu, J. Lowes, J. Berron, B. Smith, and D. Sullivan, "Spin-coating defect theory and experiments," *ECS Transactions*, vol. 60, no. 1, pp. 293–302, 2014. (Cited on page ↑28.)

[52] "Spin Coating Theory." (Cited on page ↑29.)

[53] J. Goldstein, D. E. Newbury, P. Echlin, D. C. Joy, A. D. Romig Jr, C. E. Lyman, C. Fiori, and E. Lifshin, *Scanning electron microscopy and X-ray microanalysis: a text for biologists, materials scientists, and geologists*. Springer Science & Business Media, 2012. (Cited on page ↑30.)

[54] D. Leitão, *Micro and Nano Patterned Magnetic Structures*. PhD Thesis, 2010. (Cited on page ↑31.)

[55] O. Jessensky, F. Müller, and U. Gösele, "Self-organized formation of hexagonal pore arrays in anodic alumina," *Applied Physics Letters*, vol. 72, no. 10, pp. 1173–1175, 1998. (Cited on page ↑32.)

[56] Parallax Inc., *Parallax Continuous Rotation Servo (# 900-00008)*. No. 916, 2011. (Cited on page ↑34.)

[57] Tektronix, *User Manual TDS1000- and TDS2000-Series Digital Storage Oscilloscope*. Tektronix, 2013. (Cited on page ↑41.)

[58] V. Nguyen and R. Yang, "Effect of humidity and pressure on the triboelectric nanogenerator," *Nano Energy*, vol. 2, no. 5, pp. 604–608, 2013. (Cited on page ↑45.)

[59] "Density of materials." (Cited on page ↑48.)

[60] S. R. Systems, *User Manual SR560 Low-noise preamplifier*. Stanford Research Systems, 2013. (Cited on page ↑50.)

Appendix A

Arduino Servo Program

```
#include <Servo.h>
Servo myservo;
// create servo object to control a servo
int val;
// variable
void setup()
{
  myservo.attach(9);
  // attaches the servo on pin 9 to the servo object
}
void loop()
{
  val = 0;
  // Values between 0 and 180
  // Direction: slow -> fast
  // Right: 92 -> 0
  // Left: 94 -> 180
  myservo.write(val);
  // sets the servo position according to the scaled value
  delay(10);
  // waits for the servo to get there
}
```

Appendix B

LabVIEW Interface

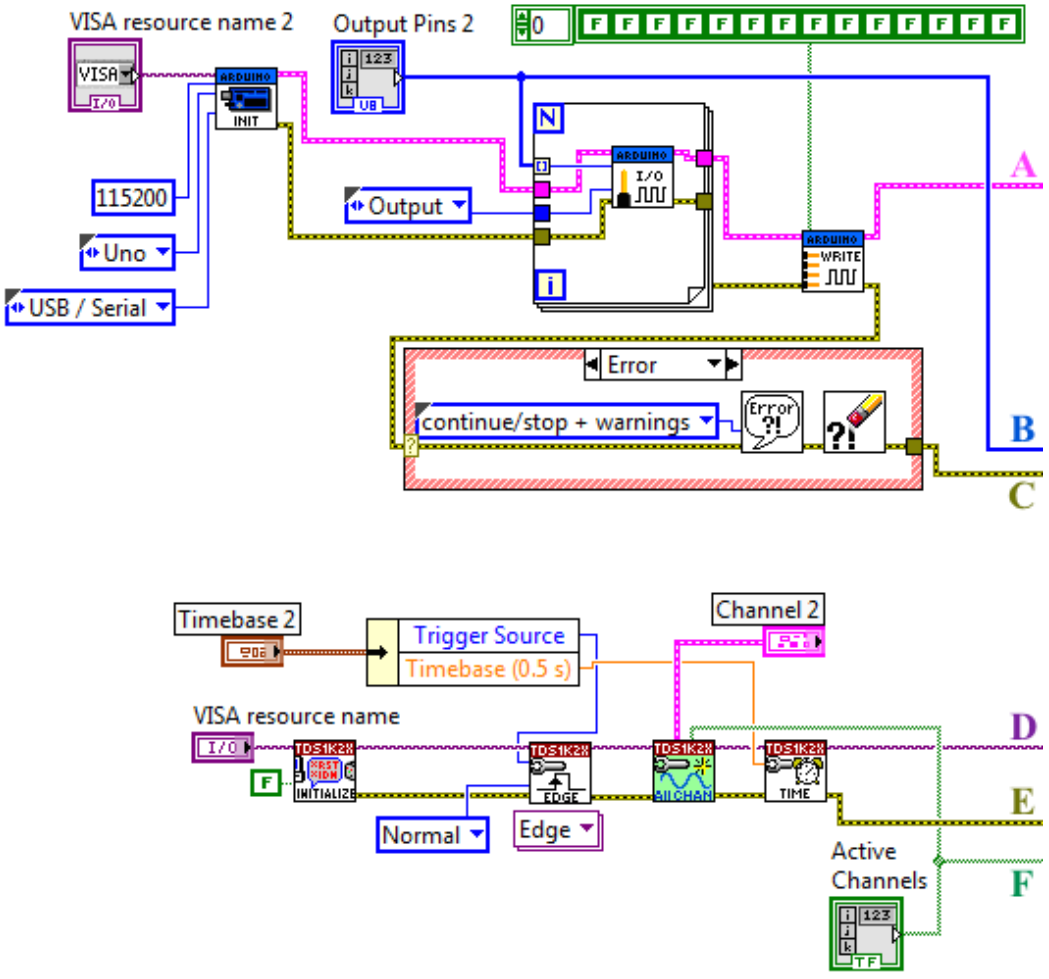


Figure B.1: Initialize LabView interface for Arduino UNO and Texmaker Oscilloscope. The other two sections of the program are presented in the next figure.

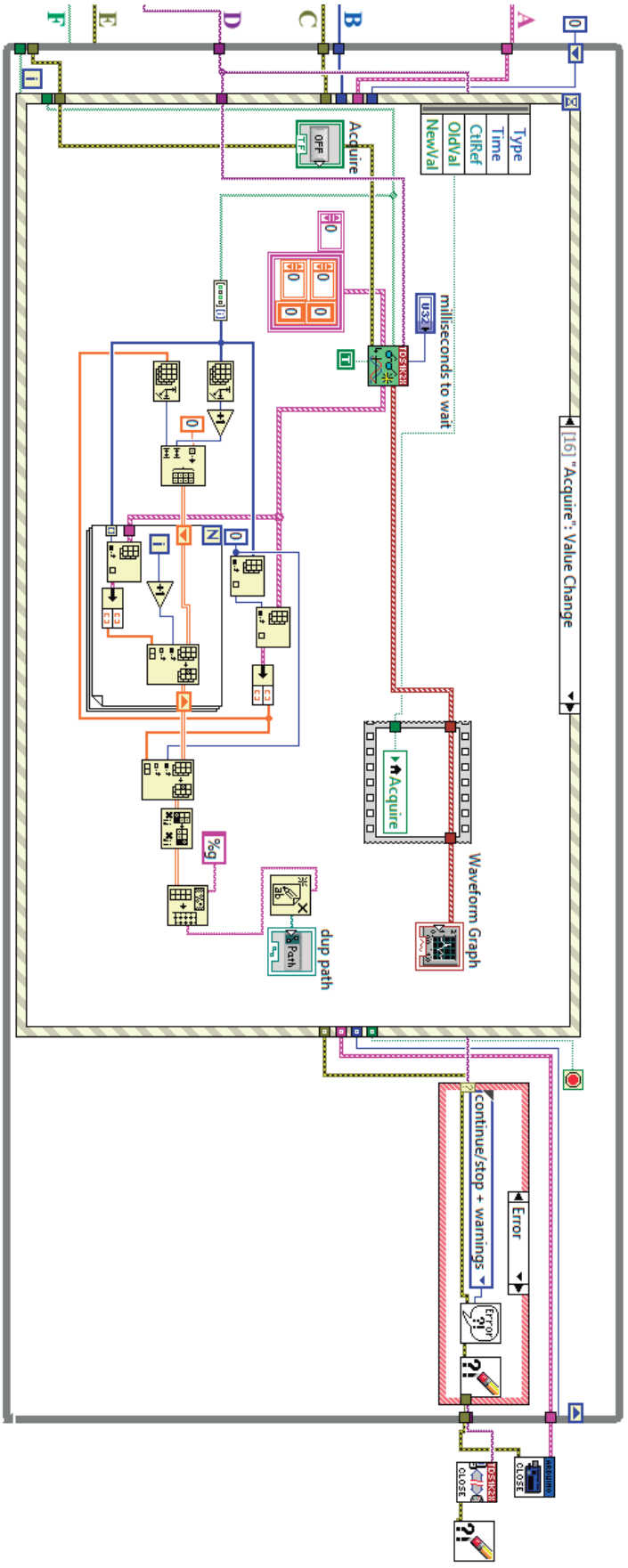


Figure B.2: Main cycle and closing LabVIEW program with the oscilloscpe event case (continuation from the previous figure).

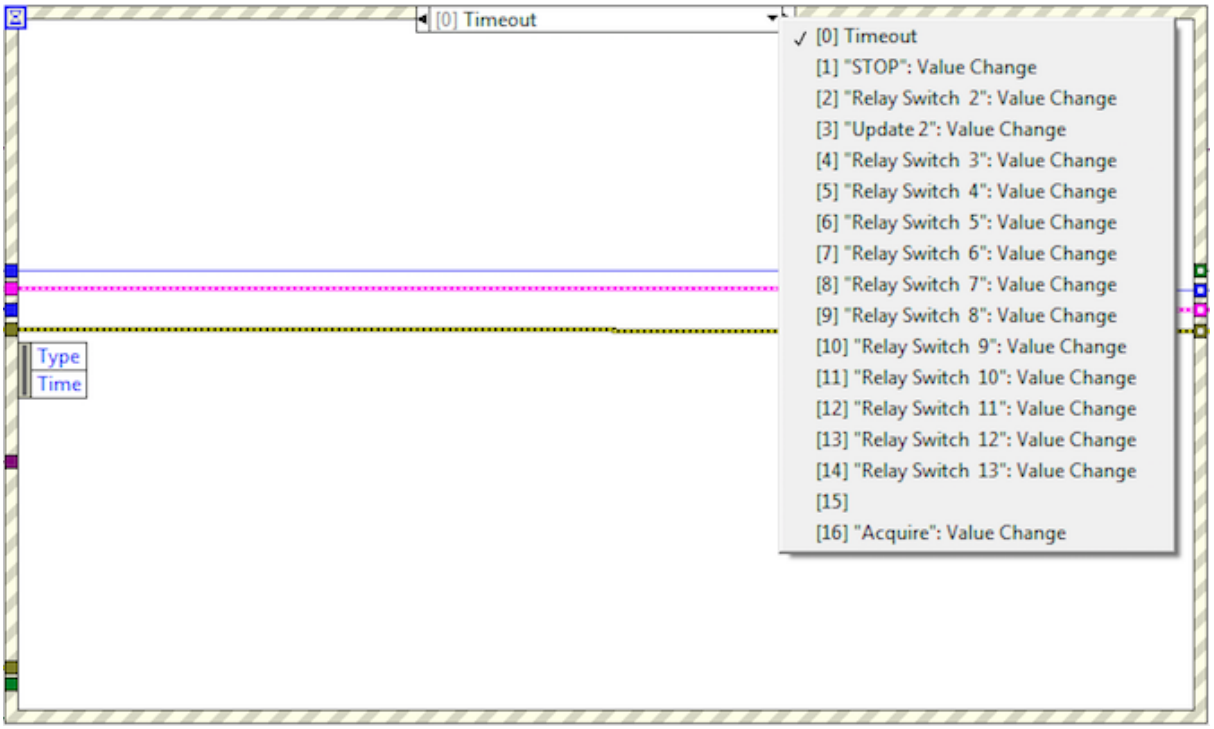


Figure B.3: Different event cases available in the LabVIEW program. The 15 event case is empty and can be used for one new event case.